DLR-IB-RM-OP-2024-37

Optimization of the Intrinsic Stiffnesses of a Robot with Variable-Stiffness-Actuators under External Disturbances with Respect to Control Effort

Masterarbeit

Luca Martin

DLR Deutsches Zentrum für Luft- und Raumfahrt

Optimization of the Intrinsic Stiffnesses of a Robot with Variable-Stiffness-Actuators under External Disturbances with Respect to Control Effort

Wissenschaftliche Arbeit zur Erlangung des Grades
M.Sc.
an der TUM School of Engineering and Design.

Themenstellender Prof. Dr.-Ing.Alin Albu-Schäffer
Chair of Sensor Based Robotic Systems and
Intelligent Assistance Systems

Betreuerin M.Sc. Marie Harder

Eingereicht von Luca Martin

Eingereicht am 01.02.2024 in Garching bei München

Erklärung

Ich versichere hiermit, dass ich die von mir eingereichte Abschlussarbeit selbstständig verfasst und keine anderen als die angegebenen Quellen und Hilfsmittel benutzt habe.

Luca Martin

München, 01.02.2024, Luca Martin

Abstract

Variable stiffness actuators (VSA) are used in robotics especially for the safe interaction with humans and because of their energy efficiency when it comes to cyclic movements. The elastic structure preserving impedance (ESPi) control framework is a control concept for VSAs. So far it is unclear how the intrinsic stiffness setting of the VSA is supposed to be set when the robot is subjected to external disturbances while controlled by the ESPi controller.

The main goal of this thesis is to utilize the variable stiffness of VSAs in order to minimize the control effort and the power input of the motor during external disturbance. The focus lies on sinusoidal disturbances with single and multiple frequencies.

To analyze the impact of the intrinsic stiffness setting on the control effort and the power input, four different optimization problems are formulated and solved to calculate optimal intrinsic stiffness settings. They cover both linear and nonlinear VSAs.

This work shows the potential of the minimization of the control effort by calculating optimal intrinsic stiffness values. Performing the minimization of the power input of the motor did not prove to have a high impact since the influence of the stiffness setting on the power input is relatively low.

It remains to be investigated whether it is possible to calculate the optimal intrinsic stiffness values in real time.

Contents

List of Figures

List of Symbols and Abbreviations

Abbreviations

DLR	Deutsches Zentrum für Luft- und Raumfahrt (German Aerospace Center)
DoF	Degree of freedom
ESP	Elastic structure preserving
ESπ	Elastic structure preserving impedance control
FSJ	Floating spring joint
SEA	Series elastic actuator
SISO	Single-input single-output
VIA	Variable impedance actuator
VIC	Variable impedance control
VSA	Variable stiffness actuator

Parameters

A_i	Amplitude of the i-th excitation frequency
B	Motor inertia
D_q	Virtual link side damping
D_η	Virtual motor side damping
E_{input}	Energy input from motor into the system
$f(K,...)$	Objective function depending on the intrinsic stiffness K
M	Link inertia
$P_{input,\varnothing}$	Average power input from motor

P_{ms}	Motor side powerport
$P_{output,\varnothing}$	Normalized power output through P_{ms}
$R_{in,out}$	Ratio between $P_{input,\varnothing}$ and $P_{output,\varnothing}$
$U_s(\phi)$	Spring potential function
q_d	Desired link coordinate
q	Link coordinate
u	Control effort
u_1	Virtual control input - linkside
u_2	Virtual control input - motorside
u_{peak}	Peak amplitude of control effort
$u_{peak,min}$	Minimal peak amplitude of control effort for fixed controlled stiffness K_q and $K = K_{opt}$
$u_{peak,min,glob}$	Minimal peak amplitude of control effort at $K_q = K_{q,opt}$ and $K = K_{opt}$
$u_{peak,norm}$	Normalized peak amplitude of control effort
η	Virtual motor coordinate
θ	Motor coordinate
$\kappa(\phi)$	Local stiffness of nonlinear spring
ξ_q	Link side damping coefficient
ξ_η	Motor side damping coefficient
τ_{ext}	External disturbance
$\tau_{ext,osc}$	Oscillating external disturbance with multiple frequency components
ϕ	Joint deflection
$\psi(\phi)$	Elastic torque
ω_{eig}	Inherent eigenfrequency
ω_{ext}	Frequency of external disturbance

Transfer functions

G_d	Disturbance model transfer function
G	Plant transfer function
G_q	Transfer function with q input and θ output

G_u	Disturbance transfer function to u
$G_{u,red}$	Reduced disturbance transfer function
G_w	Closed loop transfer function
$G_{\dot{\theta}}$	Disturbance transfer function to q
G_τ	Transfer function with τ_{ext} input and θ output
K_d	Disturbance control filter transfer function
K_r	Reference control filter transfer function
C	Controller transfer function
K_y	Feedback controller 2-Degree of freedom (DoF) control system transfer function
Q	Disturbance transfer function to q

Nonlinear stiffness parameters

σ	Stiffness setting of FSJ set by adjusting the relative rotation of the cam disks
σ_{opt}	Optimal stiffness setting which minimizes an objective function f(σ)
σ_{opt}^P	Optimal intrinsic stiffness setting which minimizes the power input $P_{input,\varnothing}$ for a specific K_q
$\sigma_{opt,glob}^P$	Optimal intrinsic stiffness setting which minimizes the average power input with $K_{q,opt}^P$
σ_{opt}^u	Optimal intrinsic stiffness setting which minimizes the peak control effort u_{peak} for a specific K_q
$\sigma_{opt,glob}^u$	Optimal intrinsic stiffness setting which minimizes the peak control effort together with $K_{q,opt}^u$
$\sigma_{opt,cor}$	Optimal stiffness setting correlated to the optimal linear stiffness K_{opt}

Linear stiffness parameters

K	Intrinsic stiffness of elastic joint

$K_{cor,\sigma}$	Intrinsic stiffness of a joint with linear stiffness corresponding to the stiffness setting σ of an FSJ for $\phi = 0$
K_{diag}	Intrinsic stiffness which lies on the diagonal of minima of $P_{input,\varnothing}$
K_{eig}	Intrinsic stiffness which leads to minimal amplitude of control effort while the link is under oscillating disturbance with one frequency ω_{ext}
K_{opt}	Optimal intrinsic stiffness which minimizes an objective function $f(K,...)$
K_{opt}^{P}	Optimal intrinsic stiffness which minimizes the average power input $P_{input,\varnothing}$ for a specific K_q
$K_{opt,glob}^{P}$	Optimal intrinsic stiffness which minimizes the average power input together with $K_{q,opt}^{P}$
K_{opt}^{u}	Optimal intrinsic stiffness which minimizes the peak control effort u_{peak} for a specific K_q
$K_{opt,glob}^{u}$	Optimal intrinsic stiffness which minimizes the peak control effort together with $K_{q,opt}^{u}$
K_q	Virtual controlled stiffness
$K_{q,opt}^{P}$	Optimal controlled stiffness which minimizes the average power input together with $K_{opt,glob}^{P}/\sigma_{opt,glob}^{P}$
$K_{q,opt}^{u}$	Optimal controlled stiffness which minimizes the peak control effort together with $K_{opt,glob}^{u}/\sigma_{opt,glob}^{u}$
$K_{q,diag}$	Controlled stiffness which lies on the diagonal of minima of $P_{input,\varnothing}$
$K_{q,opt}$	Optimial virtual controlled which minimizes an objective function $f(K,...)$
K_{spike}	Intrinsic stiffness which leads to spikes of $u_{peak}/P_{input,\varnothing}$
K_{tr}	Intrinsic stiffness at which amplitude of u higher than amplitude of τ_{ext}

1 Introduction

Ongoing research is continuously advancing the development of new actuators for robots. In the pursuit of creating actuators with capabilities similar to those of humans, there is a focus on investigating actuators with intrinsic elastic elements. The compliant actuators are a significant focus in robotics research mainly because of their mechanical robustness, their energy efficiency when it comes to cyclic movements and their good applicability for interactions with humans [1, 2]. They can be categorized into series elastic actuators (SEA) and variable stiffness actuators (VSA). While SEAs have a constant intrinsic stiffness, that of VSAs is adjustable. VSAs excel over SEAs especially when it comes to energy efficiency and maximizing the speed of the actuator [3, 4, 5, 6]. Various mechanical designs for VSAs have been proposed [7, 8, 9, 10, 11].

The optimal intrinsic stiffness settings of the VSAs during regular operations, where the elastic element is not used for explosive or non-cyclic movements (e.g. [3, 11, 12, 13]), is still an active field of study.

A variety of literature covers the variable impedance control VIC of VSAs. [14] presents a survey, comparing different VIC strategies and categorizing them in variable impedance control, variable impedance learning and variable impedance learning control. These control strategies are primarily designed to adjust the intrinsic stiffness of the VSA to establish a specific impedance for interactions with the environment. In the ESπ control strategy presented in [15], which is mainly discussed in this thesis, a differentiation between controlled and intrinsic stiffness is made. The former predominantly influences the impedance and interaction behavior and is introduced into the system by the controller. The latter is the mechanically adjustable intrinsic stiffness of the VSA. The objective of this work is to optimize this adjustable intrinsic stiffness to minimize the control effort and the power input of the actuator. This task is not addressed in the existing control strategies presented in [14].

Currently, there is no widely established control concept for setting the intrinsic stiffness during non-cyclic robotic movements or when the robot is subjected to external loads. In such cases, the potential benefits of the adjustable stiffness setting remain underutilized.

[16] showed that there is significant potential in reducing the control effort by adjusting the intrinsic stiffness of the VSA while the system is under external disturbance. Nevertheless, there is no general control law for adjusting the stiffness setting of VSAs in those scenarios.

The main goal of this thesis is to utilize the variable stiffness of VSAs in order to minimize the control effort and the power input of the motor during external disturbance, effectively making the actuator more efficient. The ESπ controller presented in [15] is used as the control concept throughout this thesis. To gain insight into the impact of varying the intrinsic stiffness in disturbance scenarios, a series of experiments is performed.

The experiments are performed on both linear and nonlinear VSAs on a system with a single degree of freedom. The focus lies on sinusoidal disturbances with singular and multiple frequencies. Finally, it is discussed whether improvements on control effort and power input justify the stiffness adjustment process.

2 Theoretical background

This chapter includes a brief overview over variable stiffness actuators and the fundamentals of control theory. Also, the basics of the ESπ control concepts are explained.

2.1 Variable stiffness actuators

While stiff actuators have exceptional positioning and tracking accuracy [2], they encounter difficulties when operating in unknown environments or interacting with humans. That is where the so called variable impedance actuators (VIA) excel [2]. There are various ways to impose impedance behavior into a system. One approach is to control a stiff actuator to behave like an impedance [2]. Another option is to incorporate an elastic element between the gear and the link which was first done in [17]. Such systems are commonly referred to as series elastic actuators (SEA). When the stiffness of the elastic element is adjustable, they are known as variable stiffness actuators (VSA), and when damping is incorporated additionally, they are called variable impedance actuators (VIA) [18]. The impedance behavior facilitates better behavior in many applications: [2, 19, 18]

- Efficiency: VIAs enhance efficiency by storing energy within their intrinsic elastic elements, particularly for dynamic movements. By this, the peak velocity can be increased. This does not work for controlled impedance, but only for intrinsic elastic elements.
- Shock-absorbing: The elastic element reduces the torque during hard impacts, thereby protecting the gearbox from damage. Additionally, it provides the controller with extra reaction time as the impact initially deforms the elastic element.

- Adaptability: Impedance behavior is beneficial in situations where continuous contact and precise force exchange are required.
- Safety: VIAs are safer when interacting with humans, particularly in collisions.

There are many different mechanical designs for VIAs [7, 8, 9, 10, 11, 20]. The mechanical design of the floating floating spring joint (FSJ) [20] developed at German Aerospace Center (DLR) is presented in the following.

The FSJ is designed to serve as a VSA in the humanoid robot David (Fig. 2.1) [20]. It is a compact, lightweight joint, suitable for a robot of human-like size and capable of reaching torques up to 67.5 Nm. The FSJ consists of two cam disks which are pressed together by the floating spring seen in Fig. 2.1. One of the disks is connected to the linkside while the other is attached to a stiffness adjustment actuator. Between the disks, there are cam rollers which are connected to the gear output shaft of the main actuator. When the joint is deflected, it causes the rollers to move radially. This radial movement along the disk profiles results in axial separation of the cam disks. The force generated by the floating spring acts as a counter force against the axial movement, which leads to the elastic behavior of the joint. An additional motor adjusts the relative rotation σ of the two cam disks, which changes the desired stiffness of the joint, effectively making the mechanism a VSA. Even though the floating spring has a constant stiffness, the mechanism leads to a nonlinear stiffness as shown in Fig. 2.2.

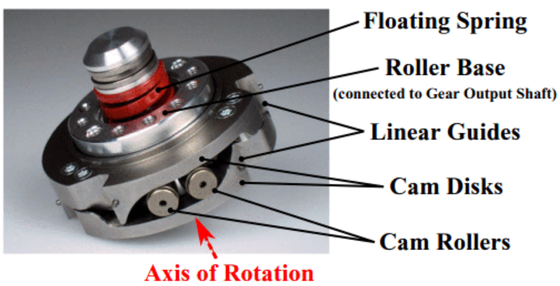

Figure 2.1: Floating spring joint mechanism [20]

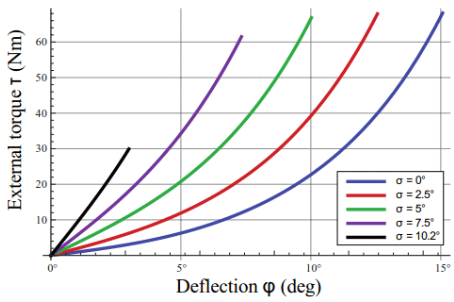

Figure 2.2: Torque vs. joint deflection of floating spring joint [20]

2.2 Control

This section first covers the essential control theory knowledge needed for this thesis. Additionally, the ESπ concept used for the control of compliantly actuated robots with nonlinear elastic elements is explained.

2.2.1 Control theory fundamentals

The basic control theory knowledge explained in this section is based on [21]. Figure 2.3 shows the structure of a one degree-of-freedom controller used for a single-input single-output (SISO) system. C and G represent the transfer functions of the controller and the system's plant, respectively. q_d and q are the input and output of the system. u is the control signal sent to the plant by the controller. G_d describes how the external disturbance τ_{ext} affects the output q.

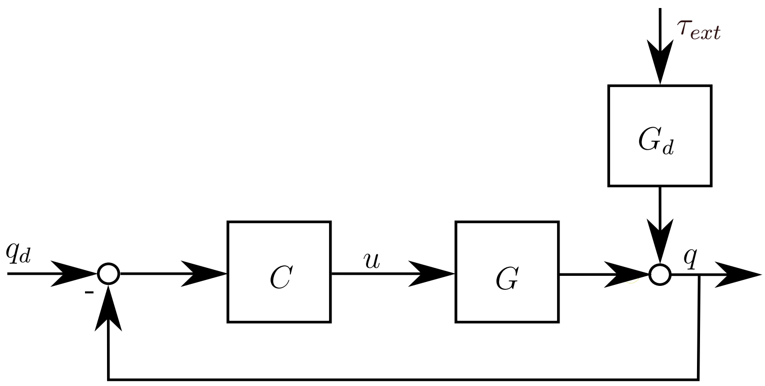

Figure 2.3: One DoF control system - adapted from [21]

The closed-loop transfer function G_w and the disturbance transfer function G_d are computed as follows:

$$G_w = \frac{G \cdot C}{1 + G \cdot C} \tag{2.1}$$

$$G_d = \frac{1}{1 + G \cdot C} \tag{2.2}$$

In certain scenarios, the incorporation of a feedforward term into the control system is beneficial to enhance tracking performance [21, 22]. This leads to a two DoF controller which can have different structures [21, 22]. One example for a two DoF controller is shown in Fig. 2.4. It is called control loop with two DoF because there are now two blocks which can be used to control the system (K_r and K_y). In theory, additional DoF's can be added to the control system if needed. This thesis covers the transformation of the ESπ controller into a three DoF standard control structure (Sections 2.2.2 and 2.2.3).

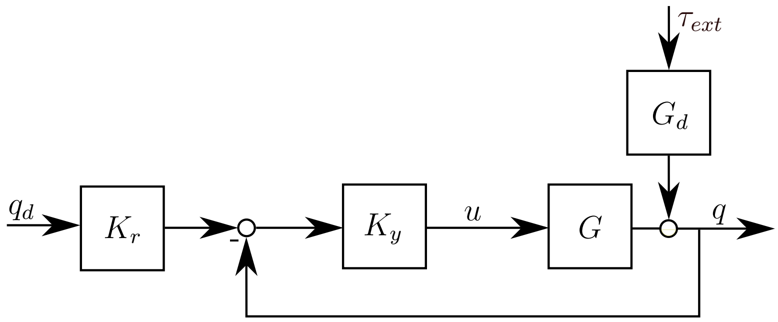

Figure 2.4: Two DoF control system - adapted from [21, 22]

2.2.2 Elastic structure preserving impedance control (ESπ)

The previously shown FSJ mechanism (2.1) is used in the DLR David robot. For the control of this joint and other VSAs, [1] proposed the elastic structure preserving (ESP) control concept. The ESπ controller presented afterwards in [15] is a slight variation of the ESP control system. Throughout this thesis, the ESπ control concept is used, so the following section explains its fundamentals.

The control concept of the ESπ framework is demonstrated using a compliant actuator with a single link. The spring connecting the rotor and the link has a constant stiffness K throughout the derivation of the control concept in order to keep the equations in the presentation of the design idea simple. It is important to note that the derivation can also be carried out analogously for nonlinear elastic elements. The concepts of ESπ for nonlinear elastic elements are briefly discussed in the next section.

The dynamics of a single link connected to a rotor with a spring with constant stiffness are shown in Fig. 2.5. u is the control parameter of the system. It imposes a generalized force which acts on the rotor inertia B. The rotor's inertia is linked to the inertia of the connecting link M via a spring with the stiffness K. θ and q represent the actuated rotor position and the unactuated link position, respectively.

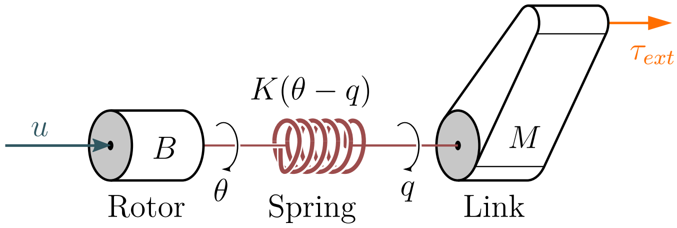

Figure 2.5: Linear-elastic joint [1]

τ_{ext} is an external torque acting on the link.
The system's dynamics are given by [1]:

$$M\ddot{q} = K(\theta - q) + \tau_{ext} \tag{2.3}$$
$$B\ddot{\theta} + K(\theta - q) = u \tag{2.4}$$

The goal of the ESπ controller is to incorporate linkside impedance behavior and motorside damping while maintaining the initial characteristics of the plant. The desired closed-loop dynamics are shown in Fig. 2.6. The according desired

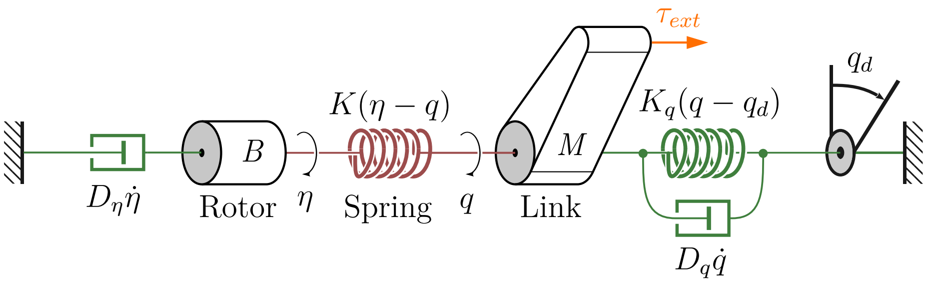

Figure 2.6: Visualization of closed-loop dynamics of the ESπ control concept - adapted from [15]

closed-loop dynamics are given by

$$M\ddot{q} = K(\eta - q) + -K_q(q - q_d) - D_q\dot{q} + \tau_{ext} \tag{2.5}$$
$$B\ddot{\eta} + K(\eta - q) = -D_\eta\dot{\eta} \tag{2.6}$$

where η is a virtual motor coordinate. It is derived by equating the link dynamics of the original system (Eq. (2.3)) and the desired dynamics (Eq. (2.5)):

$$\eta = \theta - K^{-1}\underbrace{(-K_q(q - q_d) - D_q\dot{q})}_{u_1} \tag{2.7}$$

The resulting control law u is calculated by equating Eq. (2.4) and Eq. (2.6) and inserting Eq. (2.7):

$$u = \underbrace{-D_\eta \dot{\eta}}_{u_2} + \frac{B}{K}\ddot{u}_1 + u_1 \tag{2.8}$$

Using this ESπ control law u for actuators with an elastic element like shown in Fig. 2.5 results in the desired closed loop dynamics shown in Fig. 2.6. In a static case, where $\ddot{q} = \ddot{\eta} = \dot{q} = \dot{\eta} = 0$ and $q = \eta$, the behavior of the system under external disturbance is primarily influenced by the controlled stiffness K_q. Under stronger, varying external disturbances, the system behavior gets also influenced by the intrinsic stiffness K.
The control concept can be generalized as follows [23]:

$$u = u_2 + \frac{B}{K}\ddot{u}_1 + u_1 \tag{2.9}$$

The work in [23] showed that using this control concept transforms the underactuated system (cf. Fig. 2.5) to a "quasi-fully" actuated system while preserving the original structure. "Quasi-fully" actuated means, that the noncollocated link coordinate q can be directly controlled via u_1. The generalized form of this control system is shown in Fig. 2.7. The new linkside control input u_1 enables the use of

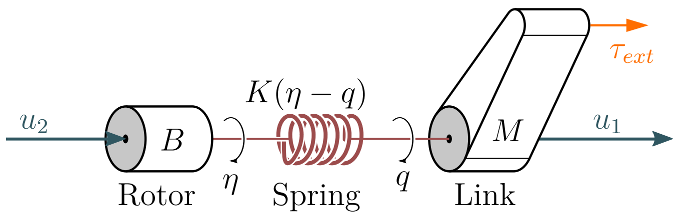

Figure 2.7: Visualization of closed-loop dynamics - adapted from [1]

classical control concepts for rigid links for compliant systems [23].

ESπ for a nonlinear elastic element

The FSJ which is used in the David robot is a nonlinear elastic joint. This means that the elastic torque $\psi(\phi)$ transmitted from the motor to the link is a nonlinear function of the joint deflection ϕ:

$$\psi(\phi) = \left.\frac{\partial U_s(\phi)}{\partial \phi}\right|_{\phi=\theta-q} \tag{2.10}$$

with $U_s(\phi)$ being the spring potential function [1]. The local stiffness $\kappa(\phi)$ is calculated with the Hessian of the spring potential function $U_s(\phi)$:

$$\kappa(\phi) = \left.\frac{\partial^2 U_s(\phi)}{\partial \phi^2}\right|_{\phi=\theta-q} = \left.\frac{\partial \psi(\phi)}{\partial \phi}\right|_{\phi=\theta-q} \tag{2.11}$$

For the nonlinear ESπ controller, u is designed such that the controlled system's dynamics are as follows:

$$M\ddot{q} + K_q(q - q_d) + D_q\dot{q} = \psi(\eta - q) + \tau_{ext} \tag{2.12}$$

$$B\ddot{\eta} + \psi(\eta - q) = -D_\eta\dot{\eta} \tag{2.13}$$

The closed-loop structure is the same as in the linear system [1].

2.2.3 Transforming ESπ to three degree-of-freedom design

One part of this thesis involves analyzing the transfer functions of the controlled system. To achieve this, the ESπ control concept must be transformed into the structure of a standard single-input single-output (SISO) control loop. This transformation was already performed in [24]. This section gives a brief summary over the transformation process.
The equations for the control inputs on the linkside (u_1) and the motorside (u_2), as defined in Eq. (2.7) and Eq. (2.8), undergo a Laplace transformation. Throughout this thesis, the ESπ regulation controller is used, so $\dot{q}_d = \ddot{q}_d = 0$. For U_2 the derivative of Eq. (2.7) is substituted into $\dot{\eta}$. Furthermore, the link dynamics seen in Eq. (2.3) are substituted into θ:

$$U_1 = -K_q\,(q - q_d) - D_q\, q\, s \tag{2.14}$$

$$\begin{aligned} U_2 &= -D_\eta\, \eta\, s = \\ &= -\left(\frac{D_\eta\, M}{K} s^3 + \frac{D_\eta\, D_q}{K}\, s^2 + \frac{D_\eta\, K_q}{K}\, s + D_\eta\, s\right)\, q \;+\; \frac{D_\eta}{K}\, s\, \tau_{ext} \end{aligned} \tag{2.15}$$

With the control law from Eq. (2.8) this leads to the final control law in the Laplace domain:

$$\begin{aligned} U = K_q\, q_d - \Bigg[&\left(\frac{D_\eta\, M}{K} + \frac{D_q\, B}{K}\right)\, s^3 + \left(\frac{B\, K_q}{K} + \frac{D_\eta\, D_q}{K}\right)\, s^2 \\ &+ \left(\frac{D_\eta\, K_q}{K} + D_\eta + D_q\right)\, s + K_q\Bigg]\, q + \frac{D_\eta}{K}\, s\, \tau_{ext} \end{aligned} \tag{2.16}$$

The control law presented in Eq. (2.16) includes the input variable q_d, the output variable q and the disturbance τ_{ext}. By defining K_y and K_z, the control law simplifies to:

$$U = K_q\, q_d - K_y\, q + K_z\, \tau_{ext} \tag{2.17}$$

Defining K_r and K_d as

$$K_r = \frac{K_q}{K_y} \tag{2.18}$$

$$K_d = \frac{K_z}{K_y} \tag{2.19}$$

results in a feedback control loop which takes q_d as feedback and subtracts it from q (compare Fig. 2.8):

$$U = K_y\, (K_d\, \tau_{ext} + K_r\, q_d - q) \tag{2.20}$$

K_r serves as a prefilter for the commanded q_d. K_y is the feedback part of the controller, which handles disturbances and model uncertainties. K_d also handles disturbances. The plant G of the system can be derived from the open-loop dynamic Eqs. (2.3) and (2.4) by performing a Laplace transformation while setting $\tau_{ext} = 0$:

$$Mqs^2 = K(\theta - q) + \tau_{ext} \tag{2.21}$$

$$B\theta s^2 + K(\theta - q) = u \tag{2.22}$$

Setting $\tau_{ext} = 0$, solving Eq. (2.22) for θ and substituting it into Eq. (2.21) leads to the plant transfer function G:

$$G = \frac{q}{u} = \frac{K}{BMs^4 + (BK + MK)s^2} \tag{2.23}$$

Similarly G_d can be derived by setting $u = 0$ in Eq. (2.22) and performing the same substitution as before:

$$G_d = \frac{q}{\tau_{ext}} = \frac{Bs^2 + K}{BMs^4 + (BK + MK)s^2} \tag{2.24}$$

G_d describes how external torques affect the link position. The presented transfer functions K_d, K_r, K_y, G and G_d form a standard control structure as presented in section 2.2.1. The structure is shown in Fig. 2.8. In case of $\tau_{ext} = 0$ or $q_d = 0$, the control system transforms into a two DoF SISO system.

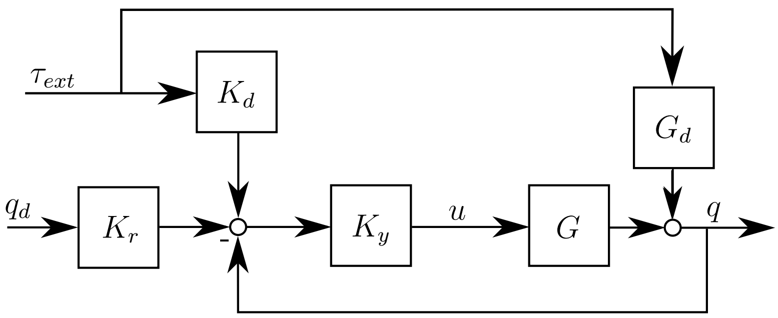

Figure 2.8: ESπ control system transformed to three DoF standard control structure - adapted from [22, 24]

3 Methodology

This chapter describes the methodology used to determine the optimal intrinsic stiffness settings for VSAs under external disturbance while being controlled with the ESπ control system described in Section 2.2.2.
To determine the optimal stiffness values, objective functions are formulated and minimized: Let $f(K,...)$ be an arbitrary objective function which should be minimized by adjusting the intrinsic stiffness K of a linear VSA controlled via ESπ. The optimal intrinsic stiffness K_{opt} calculated with Eq. (3.1) is defined as the value of K which minimizes $f(K,...)$:

$$K_{opt} = \arg\min_{K} f(K, ...) \tag{3.1}$$

Analog to that, the optimal stiffness setting σ_{opt} of the FSJ (cf. Section 2.1) controlled via ESπ is defined as:

$$\sigma_{opt} = \arg\min_{\sigma} f(\sigma, ...) \tag{3.2}$$

The sections of this chapter aim to minimize several different objective functions in order to derive optimal stiffness settings K_{opt}/σ_{opt}. Generally spoken, the regarded objective functions describe the control effort or the power input from the motor. The exact definitions of the objective functions are given in the respective sections. The optimization problems minimizing the objective functions and their respective optimal stiffness settings are summarized in table Table 3.1.

Objective function/optimal stiffness setting	Linear VSA	Nonlinear VSA
Peak control effort u_{peak}	Problem 1 Section 3.1.1	Problem 3 Section 3.2
Optimal stiffness setting K_{opt}/σ_{opt}	K_{opt}^{u}	σ_{opt}^{u}
Average power input $P_{input,\varnothing}$	Problem 2 Section 3.1.2	Problem 4 Section 3.2
Optimal stiffness setting K_{opt}/σ_{opt}	K_{opt}^{P}	σ_{opt}^{P}

Table 3.1: Overview of optimization problems and respective optimal stiffness settings

3.1 Linear elastic element

This section presents the methods for finding an optimal intrinsic stiffness for VSAs with linear elastic elements. First, the goal is to find the optimal intrinsic stiffness which minimizes the peak control effort. Then the optimal intrinsic stiffness is determined in order to minimize the average power input of the motor.

3.1.1 Minimization of peak control effort

In this section, the goal is to minimize the the objective function u_{peak}, which is defined as the maximum value of the control effort:

$$u_{peak} = \max_{t \in \mathbb{R}^+} u(t) \tag{3.3}$$

$u(t)$ is the control effort of the ESπ control concept resulting from an external disturbance τ_{ext} on the link. The calculation of the control effort u with respect to an external disturbance is described in the following. For the sake of simplicity, the analysis is performed on a single joint as shown in Fig. 2.5.
Fig. 3.1 shows the three DoF control structure derived in Section 2.2.3. Throughout this thesis, the regulation controller's set-point is established at the initial motor position q_{init}, so the system is in its equilibrium state:

$$q_d = q_{init} \tag{3.4}$$

Consequently, the transfer functions K_d and K_y can be adapted to minimize the control effort u. Equation 3.5 shows the ESπ control law for u (Eq. (2.8)) in its

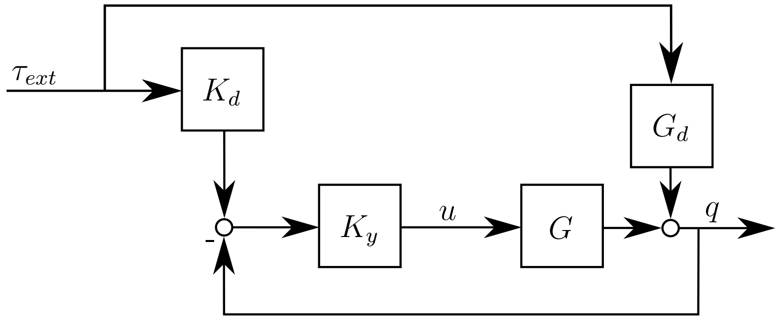

Figure 3.1: ESπ standard control structure with $q_d = q_{init}$

full form.

$$u = \underbrace{-D_q\dot{q} - K_q(q - q_d)}_{u_1} + \frac{B}{K}\underbrace{(-D_q \overset{(3)}{q} - K_q\ddot{q})}_{\ddot{u}_1} \underbrace{- D_\eta \left(\dot{\theta} + \frac{D_q\ddot{q} + K_q\dot{q}}{K}\right)}_{u_2} \tag{3.5}$$

The parameters D_q, D_η, K and K_q can be adjusted in order to minimize u. The parameter D_q is usually set in relation to M and K_q so that the linkside damping can be adapted via the damping coefficient ξ_q:

$$D_q = \xi_q \cdot 2\sqrt{K_q M} \tag{3.6}$$

In order to keep this analysis more simple, the motorside damping introduced by u_2 will not be considered, so D_η is set to zero throughout the analysis of the system with a linear elastic element.

The intrinsic stiffness K and the controlled stiffness K_q are the remaining alterable parameters in Eq. (3.5) that influence the control effort u. While K_q could theoretically be set to an arbitrary positive value, the intrinsic stiffness K depends on the specifications of the VSA. To assess the impact of K, K_q, and the external disturbance τ_{ext} on the output u, a transfer function denoted as G_u is formulated. G_u characterizes how the external load affects the control effort u. The transfer function G_u can be derived from the control structure seen in Fig. 3.1 as follows:

$$u = K_y(K_d\tau_{ext} - q) \tag{3.7}$$

$$q = G_d\tau_{ext} + G \cdot u \tag{3.8}$$

$$G_u = \frac{u}{\tau_{ext}} = \frac{K_yK_d - K_yG_d}{1 + K_yG} \tag{3.9}$$

Since $D_\eta = 0$ for this analysis, G_u reduces to:

$$G_{u,red} = \frac{u}{\tau_{ext}} = \frac{-K_y G_d}{1 + K_y G} \tag{3.10}$$

Fig. 3.2 shows the bode plots of G_u (green) and $G_{u,red}$ (blue) for one set of system parameters which are listed in the table below the figure. The negative spike in $G_{u,red}$ at 25 rad/s occurs due to the natural eigenfrequency which is determined by the motor inertia B and the intrinsic stiffness K as follows:

$$\omega_{eig} = \sqrt{\frac{K}{B}} \tag{3.11}$$

Motorside damping ($D_\eta \neq 0$) of the system introduced by u_2 results in a damped spike. The orange line in Fig. 3.2 marks the frequency $\sqrt{2} \cdot \omega_{eig}$ at which $|G_{u,red}| = 1$.

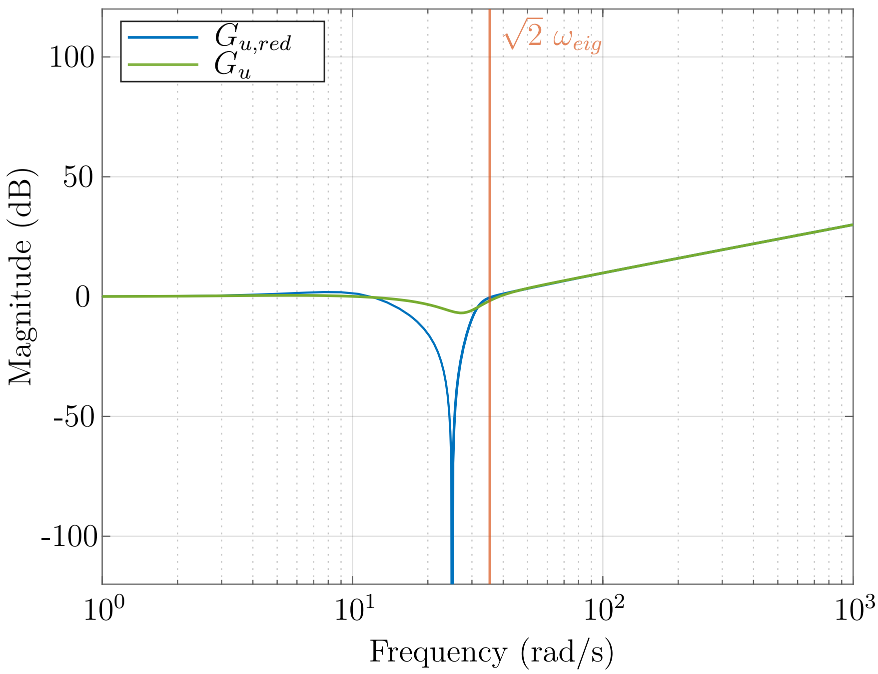

M	B	K	K_q	ξ_η	ξ_q
1 kg m^2	0.598 kg m^2	374 Nm/rad	200 Nm/rad	0 / 0.3	0.7

Figure 3.2: Bode plot of G_u and $G_{u,red}$

When the link is subjected to a sinusoidal disturbance with one frequency component, Fig. 3.2 shows that the peak amplitude of the control effort u_{peak} is minimal when the excitation frequency matches the eigenfrequency ω_{eig}. Note that ω_{eig} is independent of the controlled stiffness K_q. Since ω_{eig} can be set by changing the intrinsic stiffness K of the VSA (cf. Eq. (3.11)), it is possible to minimize the peak control effort u_{peak} by setting the intrinsic stiffness to K_{eig} which is defined as follows:

$$K_{eig} = \omega_{ext}^2 B \tag{3.12}$$

with ω_{ext} being the frequency of the external disturbance. Clearly, this optimization is constrained to the stiffness-setting boundaries of the VSA.
Under external excitation with multiple frequencies, u_{peak} cannot be determined solely by examining the transfer function G_u. The considered external disturbance $\tau_{ext,osc}$ is a superposition of i sine waves with different amplitudes A_i, frequencies $\omega_{ext,i}$ and phase shifts ϕ_i:

$$\tau_{ext,osc} = \sum_i A_i(\sin(\omega_{ext,i} \cdot t) + \phi_i) \tag{3.13}$$

The objective remains to determine the optimal intrinsic stiffness which minimizes u_{peak} with respect to the new disturbance $\tau_{ext,osc}$. Additionally, it should be investigated how the controlled stiffness K_q influences the value of K_{opt}. For that, the optimal controlled stiffness $K_{q,opt}$ is determined. This yields the subsequent optimization problem:

***Problem* 1:** Suppose the control system defined in Eqs. (2.3) and (2.4), with the controller from Eq. (2.8) subjected to an external disturbance $\tau_{ext,osc}$ of the form of Eq. (3.13).
Consider the problem of minimizing the objective function u_{peak} by adjusting the intrinsic stiffness K and the controlled stiffness K_q in order to calculate the minimal peak amplitude of the control effort $u_{peak,min,glob}$:

$$u_{peak,min,glob} = \min_{K \in [K_{min}, K_{max}], K_q \in \mathbb{R}^+} u_{peak}(K, K_q) \tag{3.14}$$

with the objective function

$$\begin{aligned} u_{peak}(K, K_q) = \max_{t \in \mathbb{R}^+} u(t) = \max_{t \in \mathbb{R}^+} \sum_i A_i \left| G_u(j\omega_{ext,i}) \right| \\ \cdot \sin(\omega_{ext,i} \cdot t + \angle G_u(j\omega_{ext,i}) + \phi_i) \end{aligned} \tag{3.15}$$

and G_u being the transfer function defined in Eq. (3.9).

For a specific controlled stiffness K_q, Eq. (3.14) simplifies to

$$u_{peak,min} = \min_{K \in [K_{min}, K_{max}], K_q \in \mathbb{R}^+} u_{peak}(K) \tag{3.16}$$

which calculates the minimal peak amplitude of the control effort $u_{peak,min}$.

The optimal intrinsic stiffness $K^u_{opt,glob}$ and controlled stiffness $K^u_{q,opt}$ that minimize the objective function in Eq. (3.15) are defined as follows:

$$(K^u_{opt,glob}, K^u_{q,opt}) = \arg \min_{K \in [K_{min}, K_{max}], K_q \in \mathbb{R}^+} u_{peak}(K, K_q) \tag{3.17}$$

The controlled stiffness K_q often cannot be chosen arbitrarily since it mainly influences the linkside impedance. For a specific controlled stiffness setting K_q, the optimal stiffness K^u_{opt} is defined as follows:

$$K^u_{opt} = \arg \min_{K \in [K_{min}, K_{max}]} u_{peak}(K) \tag{3.18}$$

For K^u_{opt}, the objective function $u_{peak}(K,K_q)$ defined in Eq. (3.15) is minimized for a specific controlled stiffness K_q.
u_{peak} consists of a sum of sine waves. The amplitude and phase of each sinusoidal component in the sum of u_{peak} is calculated using the magnitude response ($|G_u(j\omega_{ext,i})|$) and phase response ($\angle G_u(j\omega_{ext,i})$) of the transfer function G_u at the corresponding excitation frequency $\omega_{ext,i}$. The magnitude response and phase response of G_u are calculated as follows:

$$|G_u(j\omega_{ext,i})| = \sqrt{\mathrm{Re}(G_u(j\omega_{ext,i}))^2 + \mathrm{Im}(G_u(j\omega_{ext,i}))^2} \tag{3.19}$$

$$\angle G_u(j\omega_{ext,i}) = \arctan\left(\frac{\mathrm{Im}(G_u(j\omega_{ext,i}))}{\mathrm{Re}(G_u(j\omega_{ext,i}))}\right) \tag{3.20}$$

K_{min} and K_{max} are the stiffness-setting boundaries of the VSA. Problem 1 is solved with matlab. First experiments indicate that multiple local minima exist depending on the external disturbance. That is why the matlab *GlobalSearch* algorithm is used to ensure finding the global minimum $u_{peak,min,glob}$ of u_{peak}. *GlobalSearch* runs the local optimization solver *fmincon* from multiple starting points to find the global minimum of the objective function.

3.1.2 Minimization of power input

This section describes the process of determining the optimal intrinsic stiffness K_{opt} and optimal controlled stiffness $K_{q,opt}$ which minimize another objective function $P_{input,\varnothing}$. The objective function $P_{input,\varnothing}$ describes the energy introduced into the system by the motor during external disturbances while being controlled by ESπ. The derivation of $P_{input,\varnothing}$ is explained in the following.
The motor introduces energy into the system through the motorside power port P_{ms}:

$$P_{ms} = \dot{\theta} \cdot u \tag{3.21}$$

When P_{ms} is positive, the motor velocity $\dot{\theta}$ and the control effort u are both either negative or positive, indicating that the motor introduces energy into the system by accelerating the motor inertia B. Conversely, when P_{ms} is negative, the motor decelerates B, resulting in a decrease in the system's energy. Since this energy is practically unusable[1], it is disregarded in the evaluation of the energy input. This leads to the following definition of the energy input E_{input} from the motor into the system.

$$\begin{aligned} E_{input} &= \int_{t_0}^{t_1} P_{\text{ms,pos}} \, dt \\ P_{ms,pos} &= \begin{cases} P_{ms} & \text{if } P_{ms} > 0 \\ 0 & \text{if } P_{ms} \leq 0 \end{cases} \end{aligned} \tag{3.22}$$

For easier comparison between energy inputs measured over different time intervals, the energy input is normalized with respect to time. Finally, this leads to the definition of the objective function $P_{input,\varnothing}$. It describes the average power supplied by the motor while being under disturbance for Δt seconds:

$$P_{input,\varnothing} = \frac{E_{input}}{\Delta t} \tag{3.23}$$

The following section describes the derivation of the transfer functions needed to calculate the motor velocity $\dot{\theta}$ and the control effort u to compute $P_{input,\varnothing}$. The transfer

[1]This is only true if the actuator does not have energy recuperation capacity, which is generally the case for most VSAs.

function Q is determined by examining the block diagram in Fig. 3.1:

$$Q = \frac{q}{\tau_{ext}} = \frac{G_d + K_d K_y G}{1 + K_y G} \tag{3.24}$$

Q describes how the external disturbance τ_{ext} affects the output q. Laplace transforming the link dynamics (Eq. (2.3)) leads to:

$$Mqs^2 = K(\theta - q) + \tau_{ext} \tag{3.25}$$

Setting $\tau_{ext} = 0$ gives the transfer function G_q with q as the input and θ as the output (Eq. (3.26)). Similarly, setting $q = 0$ yields G_τ with τ_{ext} as the input and θ as the output (Eq. (3.27)).

$$G_q = \frac{\theta}{q} = \frac{M}{K}s^2 + 1 \tag{3.26}$$

$$G_\tau = \frac{\theta}{\tau_{ext}} = -\frac{1}{K} \tag{3.27}$$

Combining G_q, G_τ and Q yields the desired transfer function $G_{\dot{\theta}}$ which is used to calculate the output $\dot{\theta}$ with respect to the input τ_{ext}.

$$G_{\dot{\theta}} = \frac{\dot{\theta}}{\tau_{ext}} = (QG_q + G_\tau)s \tag{3.28}$$

The control effort u necessary for calculating P_{ms} is computed using the previously derived transfer function G_u (Eq. (3.9)). An overview over the used transfer functions is shown in Fig. 3.3. With these transfer functions, the energy input E_{input} and the average power input $P_{input,\varnothing}$ can be calculated with respect to an external disturbance τ_{ext} using Eq. (3.22) and (3.23).

The following presents the minimization of the average power input $P_{input,\varnothing}$ while the link is subjected to the sinusoidal disturbance $\tau_{ext,osc}$. The disturbance is a superposition of multiple sine waves and has the same form as in Eq. (3.13). Again, the optimization is carried out by calculating the optimal intrinsic and controlled stiffness values K_{opt} and $K_{q,opt}$. K is optimized within the stiffness boundaries K_{min} and K_{max} of the VSA. K_q can theoretically be set to an arbitrary positive value, so its boundaries are $[0, \infty]$. This yields another optimization problem:

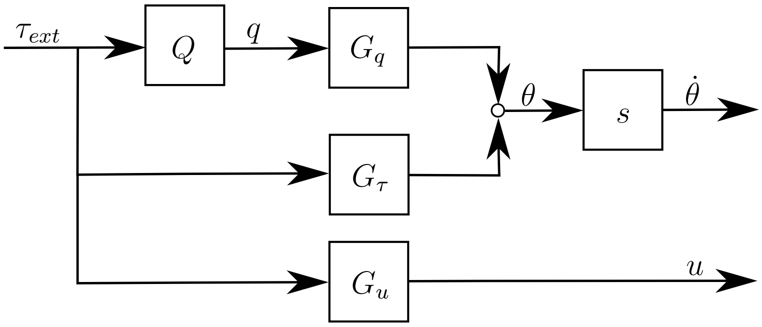

Figure 3.3: Block diagram of transfer functions used for calculating $\dot{\theta}$ and u

***Problem* 2:** Suppose the control system defined in Eqs. (2.3) and (2.4), with the controller from Eq. (2.8) subjected to an external disturbance $\tau_{ext,osc}$ of the form of Eq. (3.13).
Consider the problem of minimizing the objective function $P_{input,\varnothing}$ by adjusting the intrinsic stiffness K and the controlled stiffness K_q in order to calculate the minimal power input from the motor:

$$\min_{K \in [K_{min}, K_{max}], K_q \in \mathbb{R}^+} P_{input,\varnothing}(K, K_q)$$

with $P_{input,\varnothing}$ defined in Eq. (3.23)

The optimal intrinsic stiffness $K^P_{opt,glob}$ and controlled stiffness $K^P_{q,opt}$ that minimize the objective function $P_{input,\varnothing}$ in Problem 2 are defined as follows:

$$(K^P_{opt,glob}, K^P_{q,opt}) = \arg \min_{K \in [K_{min}, K_{max}], K_q \in \mathbb{R}^+} P_{input,\varnothing}(K, K_q) \tag{3.29}$$

For a specific controlled stiffness K_q, the optimal intrinsic stiffness K^P_{opt} is defined as follows:

$$K^P_{opt} = \arg \min_{K \in [K_{min}, K_{max}]} P_{input,\varnothing}(K) \tag{3.30}$$

The angular velocity of the motor $\dot{\theta}$ and the commanded torque u which result from the external disturbance $\tau_{ext,osc}$ are needed for the calculation of $P_{input,\varnothing}$ (c.f. Eq. (3.21)-(3.23)). $\dot{\theta}$ and u are calculated using the respective transfer functions

G_u and $G_{\dot{\theta}}$(c.f. Eqs. (3.9) and (3.28)):

$$\dot{\theta} = \sum_i A_i \left|G_{\dot{\theta}}(j\omega_{ext,i})\right| \cdot \sin(\omega_{ext,i} \cdot t + \angle G_{\dot{\theta}}(j\omega_{ext,i}) + \phi_i) \tag{3.31}$$

$$u = \sum_i A_i \left|G_u(j\omega_{ext,i})\right| \cdot \sin(\omega_{ext,i} \cdot t + \angle G_u(j\omega_{ext,i}) + \phi_i) \tag{3.32}$$

Problem 2 is solved with matlab using the *GlobalSearch* algorithm, since first experiments indicated that for certain disturbances, local minima of E_{input} are present. *fmincon* is used as the local optimization solver.

3.2 Nonlinear elastic element

This section addresses finding an optimal intrinsic stiffness setting for VSAs with nonlinear elastic elements. Similar to the previously described linear case, it describes the methodology for determining the optimal intrinsic stiffness setting that minimizes the objective functions u_{peak} (cf. Eq. (3.3)) and $P_{input,\varnothing}$ (cf. Eq. (3.23)) when the link is subjected to an external disturbance.

Due to the nonlinearity of the system, transfer functions cannot be used to calculate u_{peak} and $P_{input,\varnothing}$. Therefore, a Simulink model of the dynamics of a one DoF system and the ESπ controller is created to calculate u_{peak} and $P_{input,\varnothing}$ for different intrinsic and controlled stiffness settings.

The nonlinear spring characteristics of an FSJ are used in the Simulink model (cf. Section 2.1). To adjust the intrinsic stiffness of an FSJ, an additional motor changes the relative rotation σ of two cam disks. The parameter σ ranges from 0° (lowest stiffness setting) to 10° (highest stiffness setting). Fig. 3.4 shows the intrinsic stiffness $\kappa(\phi)$ (cf. Eq. (2.11)) versus the deflection of the spring ϕ defined by:

$$\phi = \theta - q \tag{3.33}$$

It is important to note that the physical FSJ has a maximum joint deflection due to the saturation of the spring [20]. The maximum joint deflection decreases as σ increases. Therefore, for high deflection values, the high stiffness values shown in Fig. 3.4 may not be reachable on the physical FSJ, depending on σ. In the nonlinear case, the intrinsic stiffness K cannot be used as an optimization parameter because

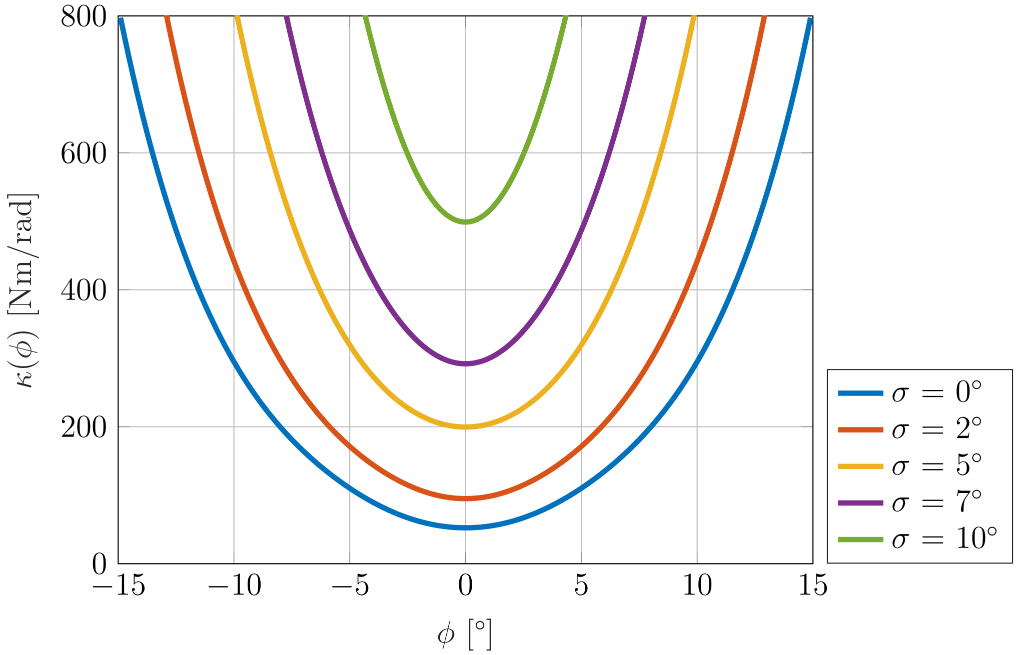

Figure 3.4: Local stiffness of an FSJ versus link deflection ϕ

it changes with the joint deflection and thus with the external disturbance. Instead, the optimization parameter for the nonlinear case is the relative rotation of the cam disks σ. For the same reason, the linkside damping D_q cannot be calculated via Eq. (3.6). Instead, the damping factor is calculated with respect to the joint deflection $\phi = \theta - q$:

$$D_q = \xi_q \cdot 2\sqrt{\kappa(\theta - q)M} \tag{3.34}$$

$\kappa(\phi)$ is the local stiffness of the nonlinear FSJ. Similarly, the motorside damping D_η is varied with the damping factor ξ_η and calculated by:

$$D_\eta = \xi_\eta \cdot 2\sqrt{\kappa(\theta - q)B} \tag{3.35}$$

The optimal stiffness setting σ_{opt} defined in Eq. (3.2) is calculated to minimize the objective functions u_{peak} and $P_{input,\varnothing}$ (cf. Eq. (3.3) and (3.23)). This poses the following optimization problems:

***Problem* 3:** Suppose the control system defined in Eqs. (2.3) and (2.4) ($\kappa(\phi)$ instead of $K(\theta - q)$ because of nonlinearity), with the controller from Eq. (2.8) subjected to an external disturbance $\tau_{ext,osc}$ of the form of Eq. (3.13).
Consider the problem of minimizing the objective function u_{peak} by adjusting the intrinsic stiffness setting σ and the controlled stiffness K_q in order to calculate the minimal amplitude of the control effort $u_{peak,min,glob}$:

$$u_{peak,min,glob} \quad = \min_{\sigma \in [0°,10°], K_q \in \mathbb{R}^+} u_{peak}(\sigma, K_q)$$

u_{peak} is defined in Eq. (3.3).

u_{peak} is calculated via a Simulink simulation. The optimal intrinsic stiffness $\sigma^u_{opt,glob}$ and controlled stiffness $K^u_{q,opt}$ that minimize the objective function in Eq. (3.3) are defined as follows:

$$(\sigma^u_{opt,glob},\ K^u_{q,opt}) = \arg \min_{\sigma \in [0°,10°], K_q \in \mathbb{R}^+} u_{peak}(\sigma, K_q) \tag{3.36}$$

For a specific controlled stiffness K_q, the optimal intrinsic stiffness setting is defined as σ^u_{opt}

$$\sigma^u_{opt} = \arg \min_{\sigma \in [0°,10°]} u_{peak}(\sigma) \tag{3.37}$$

with u_{peak} defined in in Eq. (3.3).

***Problem* 4:** Suppose the control system defined in Eqs. (2.3) and (2.4) ($\kappa(\phi)$ instead of $K(\theta - q)$), with the controller from Eq. (2.8) subjected to an external disturbance $\tau_{ext,osc}$ of the form of Eq. (3.13).
Consider the problem of minimizing the objective function $P_{input,\varnothing}$ by adjusting the intrinsic stiffness setting σ and the controlled stiffness K_q to calculate the minimal power input from the motor:

$$\min_{\sigma \in [0°,10°], K_q \in \mathbb{R}^+} P_{input,\varnothing}(\sigma, K_q)$$

with $P_{input,\varnothing}$ defined in Eq. (3.23).

The minimal value of $P_{input,\varnothing}$ is calculated via a Simulink simulation.
The optimal intrinsic stiffness $\sigma^P_{opt,glob}$ and controlled stiffness $K^P_{q,opt}$ that minimize

the objective function $P_{input,\varnothing}$ in Problem 4 are defined as follows:

$$(\sigma^P_{opt,glob}, K^P_{q,opt}) = \arg \min_{\sigma \in [0°,10°], K_q \in \mathbb{R}^+} P_{input,\varnothing}(\sigma, K_q) \tag{3.38}$$

For a fixed controlled stiffness K_q, the optimal intrinsic stiffness is defined as σ^P_{opt}:

$$\sigma^P_{opt} = \arg \min_{\sigma \in [0°,10°]} P_{input,\varnothing}(\sigma) \tag{3.39}$$

For both Problem 3 and Problem 4, σ is optimized within its stiffness setting boundaries $\sigma \in [0°, 10°]$. K_q can theoretically be set to an arbitrary positive value, so its boundaries are $[0, \infty]$. $P_{input,\varnothing}$ and u_{peak} which result from the disturbance $\tau_{ext,osc}$ are calculated using the Simulink model.
For both optimization problems, the transient state after inducing the external disturbance is neglected and only the steady state is considered. This makes the nonlinear case more comparable to the linear case, since the use of transfer functions in the linear case neglects the transient state as well.

4 Results

This chapter summarizes the knowledge acquired from the application of the procedures presented in Chapter 3. Section 4.1 covers the results for joints with linear elastic elements, while Section 4.2 presents the results for joints with nonlinear elastic elements. Table 4.1 lists the parameter values that were used for the following analyses and simulations. A linkside damping factor of $\xi_q = 0.7$ is used since it showed the best overall performance for practical applications.

Link inertia M	Motor inertia B	Linkside damping factor ξ_q	Motorside damping factor ξ_η
$1\ kg\ m^2$	$0.598\ kg\ m^2$	0.7	0/0.3

Table 4.1: Parameter settings for experiments

4.1 Experiments with linear elastic element

The following section presents the results for a linear elastic element based on theory and simulation. Initially, the minimization of the peak amplitude of the control effort u_{peak} is addressed according to Problem 1 followed by the minimization of the average power input $P_{input,\varnothing}$ according to Problem 2. Various plots are included to illustrate the peak amplitude of the control effort u_{peak} for different disturbance scenarios. They will be analyzed to derive heuristics for setting the intrinsic stiffness K in order to minimize u_{peak} or $P_{input,\varnothing}$. Additionally, the influence of the controlled stiffness K_q on u_{peak} and $P_{input,\varnothing}$ is discussed.
For the calculation of u_{peak} and $P_{input,\varnothing}$ for a linear elastic element, a Simulink

simulation is not necessary since they can be directly calculated via the transfer functions G_u and $G_{\dot{\theta}}$ (Section 3.1) which determine the steady state. Therefore the transient behavior of the system is not analyzed. G_u and $G_{\dot{\theta}}$ needed for the calculation of the peak amplitude of the control effort u_{peak} and the average power input $P_{input,\varnothing}$ were validated via the Simulink model of the ESπ controller.

4.1.1 Experiments on minimization of peak control effort

This section examines the effect of the intrinsic and controlled stiffness K and K_q on the peak amplitude of the control effort u_{peak} when subjected to sinusoidal disturbances as previously defined in Problem 1.

Excitation with one frequency component

First, the influence of sinusoidal disturbances with one frequency component on u_{peak} is discussed.
Fig. 4.1 shows the surface plot of the peak amplitude of the control effort u_{peak} over the intrinsic and controlled stiffness K and K_q for sinusoidal excitation τ_{ext} with a frequency of 2 Hz and an amplitude of 10 Nm. The values of u_{peak} were calculated using the transfer function G_u and Eq. (3.15). The green line in the plot shows the minimal peak amplitude $u_{peak,min}$ calculated with Eq. (3.16) in Problem 1 over K_q. For this disturbance, the optimal stiffness K^u_{opt} remains constant at 94.4 Nm/rad regardless of the choice of K_q. This confirms Eq. (3.12) for K_{eig}, as discussed in Section 3.1.1, which states that $u_{peak,min}$ correlates with the eigenfrequency ω_{eig} of the system. When the intrinsic stiffness K is set to K_{eig}, u_{peak} is close to zero.
Fig. 4.2 shows the plot of the external disturbance torque τ_{ext} and the spring force $K_{eig}(\theta - q)$ for this example with the intrinsic stiffness set to K_{eig}. The torques oscillate out of phase by exactly 180° with the same amplitude, resulting in no movement of the link coordinate q (red line in Fig. 4.3). Examining Eqs. (2.7) and (2.8) for $\dot{q} = q = 0$ and no motorside damping ($D_\eta = 0$) shows that u_{peak} is also zero in this case. The motor coordinate θ moves 180° out of phase with the external disturbance τ_{ext} (blue line in Fig. 4.3).
Calculating u_{peak} for multiple different disturbances with different excitation frequencies resulted in similar plots with the minimal peak amplitude $u_{peak,min}$ at $K^u_{opt} = K_{eig}$. For all disturbances, u_{peak} always increases significantly for small

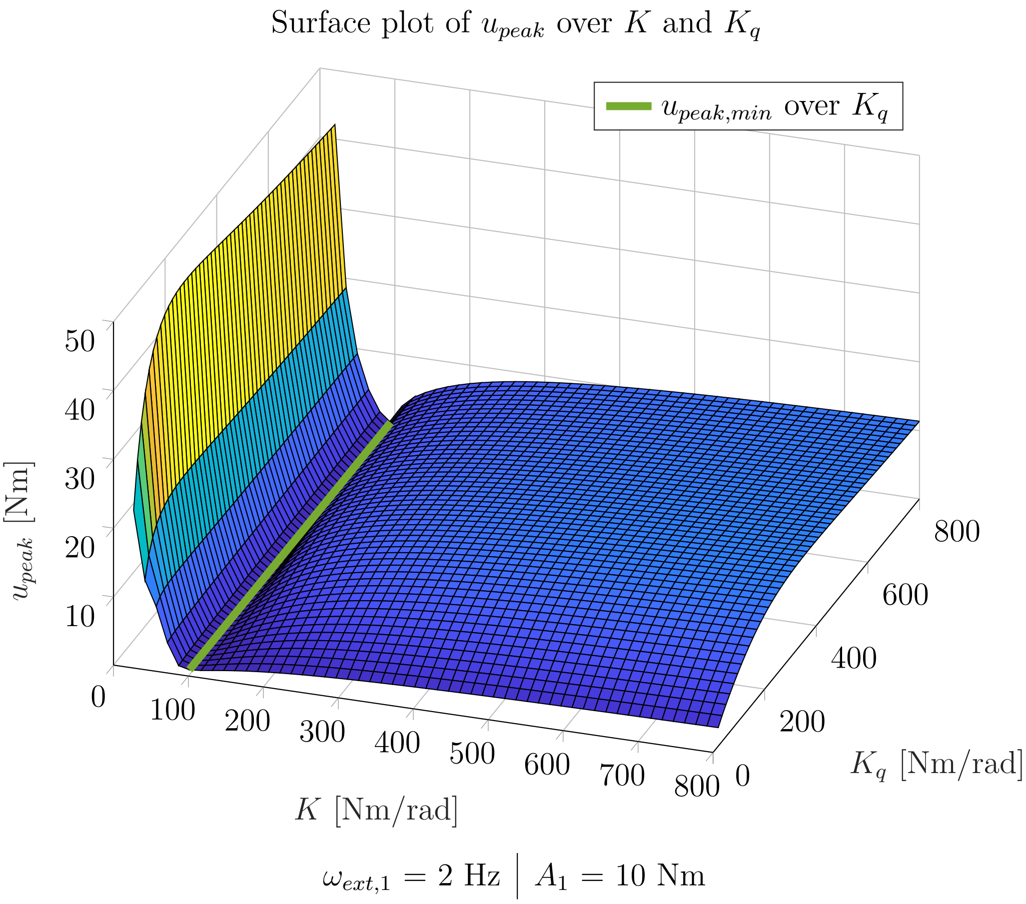

Figure 4.1: Minimization of control effort - excitation with a single frequency

intrinsic stiffness values below K_{eig}. When the intrinsic stiffness is below K_{eig}, the eigenfrequency ω_{eig} of the system is lower than the excitation frequency ω_{ext}. Examining the bode plot (Fig. 3.2), it can be observed that $|G_{u,red}|$ rises with 20 dB/decade after $\omega = \sqrt{2} \cdot \omega_{eig}$. This explains the strong rise of u_{peak} below K_{eig}. The orange line in Fig. 3.2 marks the frequency at which $|G_{u,red}| = 1$ implying that τ_{ext} and u have the same amplitude at this frequency. For an arbitrary disturbance, the corresponding stiffness threshold K_{tr} at which the amplitudes of τ_{ext} and u match is calculated using:

$$K_{tr} = \frac{\omega_{ext}^2}{2} \cdot B \tag{4.1}$$

For intrinsic stiffness values $K<K_{tr}$, the peak amplitude of the control effort u_{peak} is higher than that of τ_{ext}. For $K>K_{eig}$, u_{peak} rises comparably slowly and does not diverge to infinity. In scenarios where ω_{ext} is unknown, it is suggested to set K to a high value since it is less likely to result in very high amplitudes of the control effort u_{peak}.

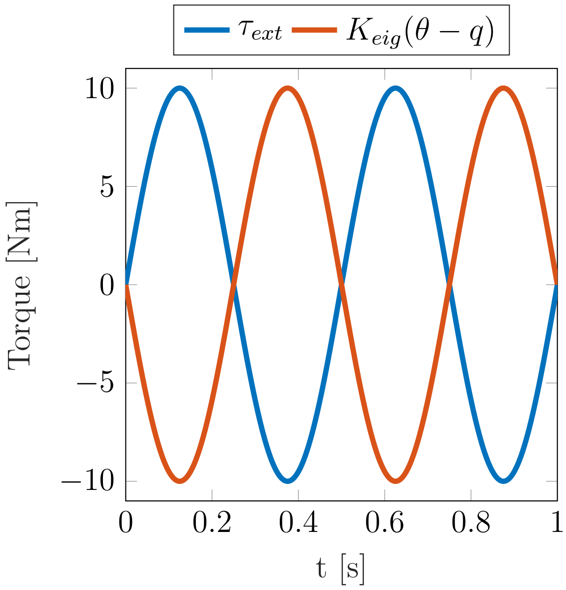

Figure 4.2: External disturbance τ_{ext} oscillates 180° out of phase with spring force

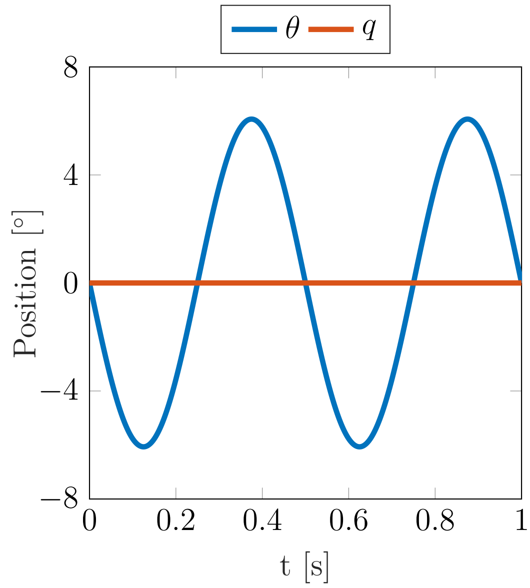

Figure 4.3: Link coordinate q and motor coordinate θ when $K = K_{eig}$

Excitation with multiple frequency components

In this section, the minimization of the peak amplitude u_{peak} for the external disturbance with multiple frequency components is addressed according to Problem 1. The considered external disturbances consist of multiple superimposed sine waves with different frequencies and phase shifts (compare Eq. (3.13)). The resulting control effort u and its peak amplitude u_{peak} are calculated with Eqs. (3.15), (3.19) and (3.20), again using the derived transfer function G_u.

Fig. 4.4 shows the plot for an external disturbance with two frequencies $\omega_{ext,1} = 3$ Hz and $\omega_{ext,2} = 4.5$ Hz, each having an amplitude of 1 Nm. The z-axis is scaled logarithmically to facilitate the analysis. Similar to excitation with one frequency, u_{peak} rises faster for low intrinsic stiffness values than for high ones. Solving Problem 1 within the stiffness boundaries $K \in [50, 800]$ and $K_q \in [50, \infty]$ results

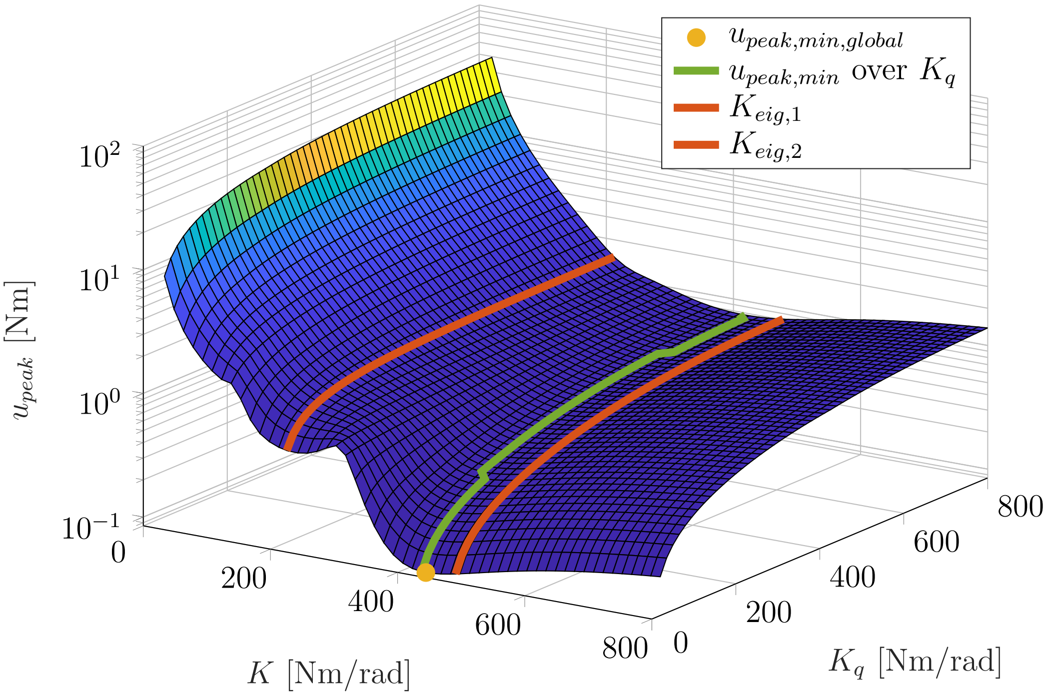

$\omega_{ext,1} = 3$ Hz | $A_1 = 1$ Nm
$\omega_{ext,2} = 4.5$ Hz | $A_2 = 1$ Nm

Figure 4.4: Minimization of control effort - excitation with multiple frequencies

in the minimum amplitude of the control effort $u_{peak,min,glob} = 0.085$ Nm. The optimal intrinsic and controlled stiffness values $K^u_{opt,glob}$ and $K^u_{q,opt}$ are calcualted in Eq. (3.17). They lie at $K^u_{opt,glob} = 431$ Nm/rad and $K^u_{q,opt} = 50$ Nm/rad leading to $u_{peak,min,glob}$ which is shown in Fig. 4.4 as the yellow dot.
The optimal controlled stiffness $K^u_{q,opt}$ lies at the lower boundary of the optimization range. This was the case for all experiments performed with respect to different external disturbances. However, K_q can usually not be chosen arbitrarily in practical applications since it influences the interaction behavior of the link. That is why for the practical case, the optimal intrinsic stiffness K^u_{opt} defined in Eq. (3.18) is usually of higher interest.
For the excitation with one frequency, finding K^u_{opt} is straight forward since it is directly related to the eigenfrequency of the system. For excitations with multiple frequencies, solving Problem 1 is required to calculate $K^u_{opt,glob}/K^u_{opt}$. In Fig. 4.4, the values of K_{eig} of the respective frequency components are represented by the

red lines. They are calculated using Eq. (3.12) by inserting the frequencies $\omega_{ext,i}$ of the disturbance $\tau_{ext,osc}$.
The green line shows the $u_{peak,min}$ over K_q. Similar to the previous example, K_{opt}^u is constant over K_q. $u_{peak,min}$ lies in between $K_{eig,1}$ and $K_{eig,2}$ over the full range of K_q. This is an interesting finding since it can be used as a heuristic for setting the intrinsic stiffness K without performing an optimization. Multiple experiments with different excitations were performed to confirm this heuristic.
Another example is shown in Fig. 4.5 for disturbance with lower frequencies ω_{ext} of 1 Hz and 2 Hz. Again, K_{opt}^u lies in between of $K_{eig,1}$ and$K_{eig,2}$ and stays nearly

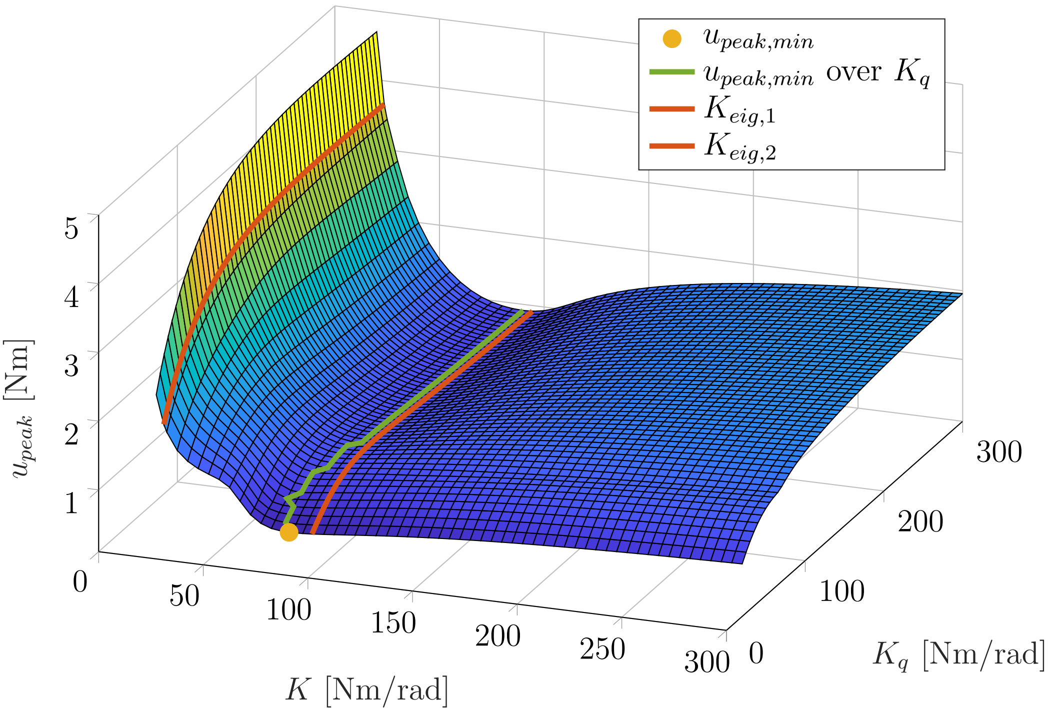

$\omega_{ext,1} = 1$ Hz	$A_1 = 1$ Nm
$\omega_{ext,2} = 2$ Hz	$A_2 = 1$ Nm

Figure 4.5: Optimal stiffness K_{opt} closer to $K_{eig,2}$ for equal amplitudes A_i

constant over K_q. The small deviations of K_{opt}^u in the lower K_q range originate from the damped spikes in the bode plot of G_u, which is explained in Section 4.1.1 - Damping variation. It is noteworthy that K_{opt}^u is closer to the higher value of K_{eig} over the full range of K_q in both examples. This was the case for all performed experiments with equal excitation amplitudes A_i. Therefore, choosing the highest

K_{eig} as the intrinsic stiffness K for excitations with similar amplitudes can serve as a heuristic. Although there is no general rule for predicting how close K^u_{opt} will be to K_{eig}, using this heuristic increases the probability to be close to K^u_{opt}.
When the excitation amplitudes A_i differ, this influences K^u_{opt}. Fig. 4.6 shows the plots of the peak amplitude of the control effort u_{peak} for the same disturbance τ_{ext} with two excitation frequencies of 1.2 Hz and 3 Hz. Only the amplitudes A_i differ between both examples. $u_{peak,min}$ calculated by solving Problem 1 is marked with the red crosses. The controlled stiffness is set to $K_q =$ 300 Nm/rad for both cases.

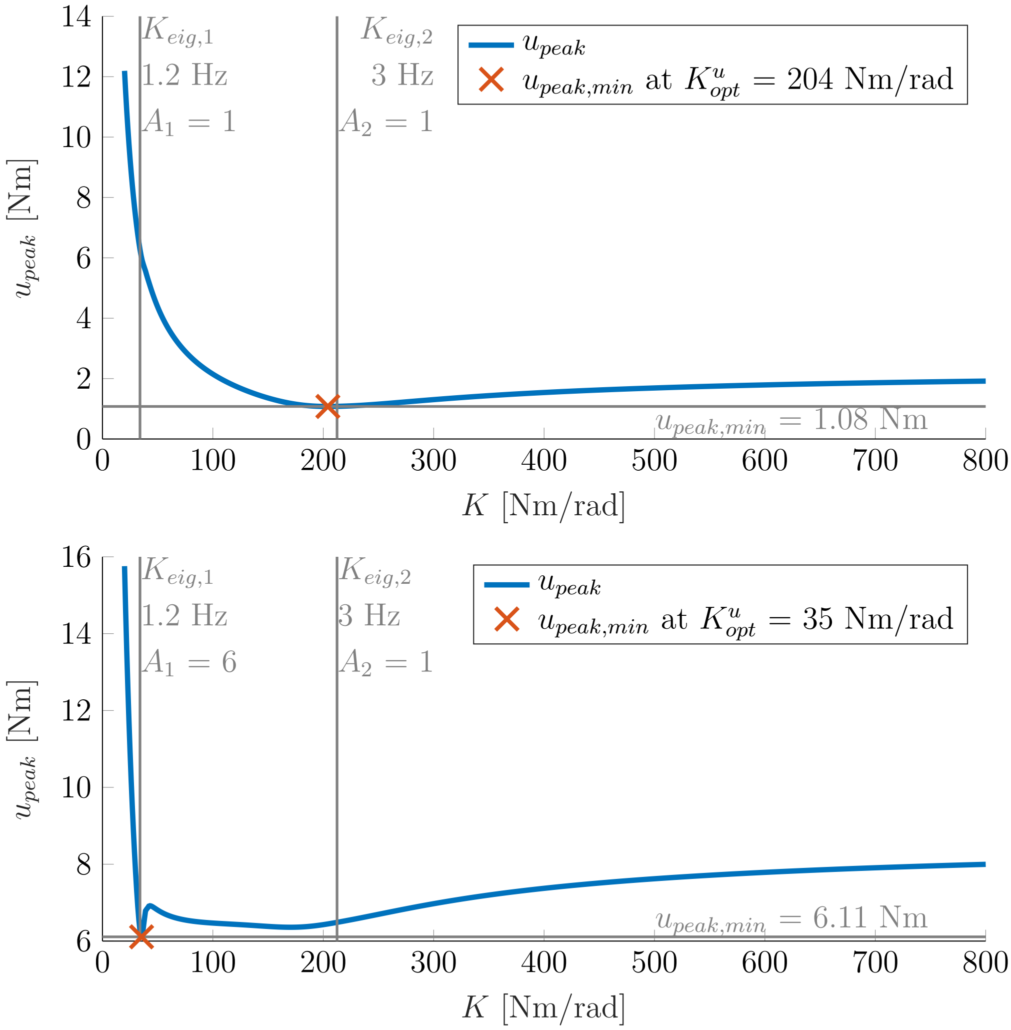

Figure 4.6: Variation of the amplitudes - u_{peak} over K for K_q = 300 Nm/rad

Increasing the amplitude A_1 of the lower frequency by a factor of six results in a decrease in K^u_{opt} so K^u_{opt} moves closer to $K_{eig,1}$. This can result in local minima (see Fig. 4.6(b)) which is why the global optimizer is used for the experiments (cf. Section 3.1.1).

Fig. 4.7 shows the course of the optimal intrinsic stiffness K^u_{opt} over K_q for the same disturbance as in Fig. 4.6(b). K^u_{opt} jumps from being close to $K_{eig,1}$, closer

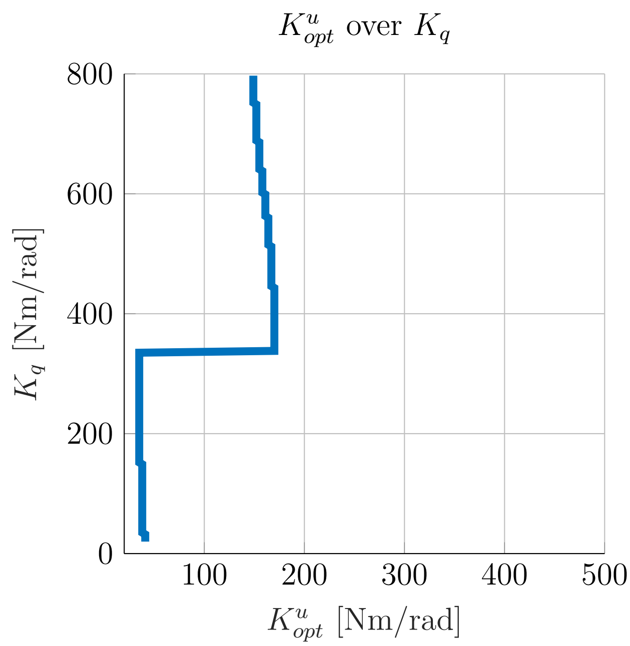

$$\begin{array}{r|l} \omega_{ext,1} = 1.2 \text{ Hz} & A_1 = 6 \text{ Nm} \\ \omega_{ext,2} = 3 \text{ Hz} & A_2 = 1 \text{ Nm} \end{array}$$

Figure 4.7: K^u_{opt} not constant over K_q

to $K_{eig,2}$ at $K_q \approx$ 335 Nm/rad. This shows that differing amplitudes of the excitation frequencies can lead to K^u_{opt} not being constant over K_q. Determining the controlled stiffness K_q at which the jump occurs remains a promising topic for future research.

Efficient solution of optimization problem

To be able to find K^u_{opt} in real time and react quickly to external disturbances, it is necessary to solve Problem 1 for a specific controlled stiffness K_q quickly. Solving

the optimization problem using the Matlab *GlobalSearch* algorithm takes fairly long because it uses many different starting points. This makes it unusable for real-time applications.
Since all performed experiments showed that K^u_{opt} lies somewhere between the highest and the lowest K_{eig}, it is possible to reduce the optimization time by using only the $K_{eig,i}$ values as starting points for an optimization with a local solver. Fig. 4.8 shows an example for the optimization. $K_{eig,1} = 34$ Nm and $K_{eig,2} = 212.4$ Nm are used as starting points. Two different minima are found (see red crosses in Fig. 4.8), successfully finding the optimal intrinsic stiffness at $K^u_{opt} = 40$ Nm/rad.

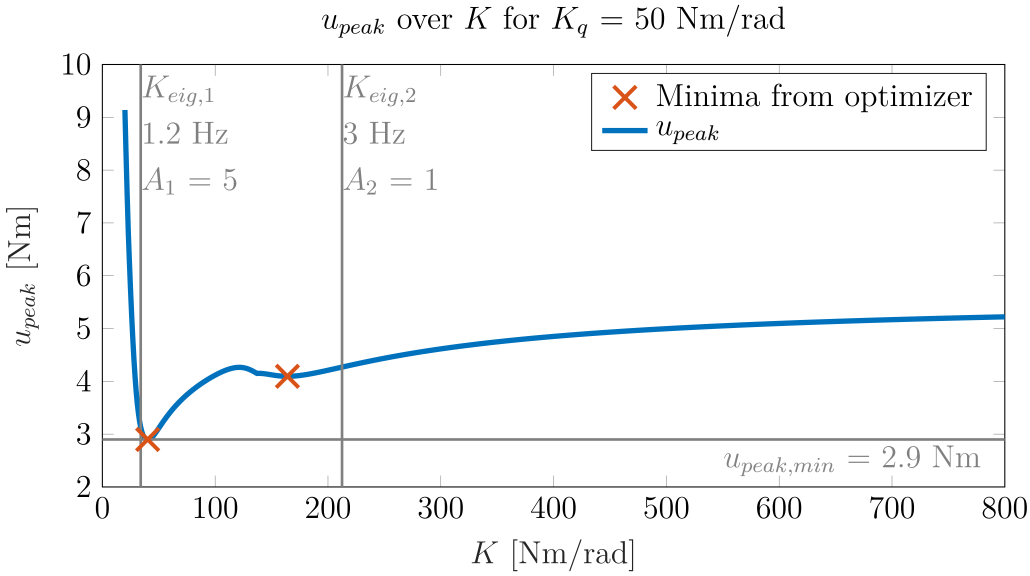

Figure 4.8: Optima found with $K_{eig,i}$ as starting points

By reducing the starting points, the optimization process becomes significantly faster (by a factor ≈ 100) compared to the previously used *GlobalSearch* algorithm. Without further optimizations to the script the calculation time for an optimization problem with two starting points was around 0.4 s on average[1]. This duration can likely be further reduced with more adjustments to the optimization problem. It remains to be investigated whether this change allows for real time optimization.

[1]The optimizations were performed on an Intel Core i5 - 12400F (2.5GHz) processor using 16 GB of RAM running on Windows 11.

Damping variation

The optimal intrinsic and controlled stiffness values $K^u_{opt,glob}/K^u_{opt}$ and $K^u_{q,opt}$ are also influenced by the linkside damping factor ξ_q. Fig. 4.9 shows the bode plot for varying ξ_q. For $\xi_q = 0$ there are two positive spikes which are damped with

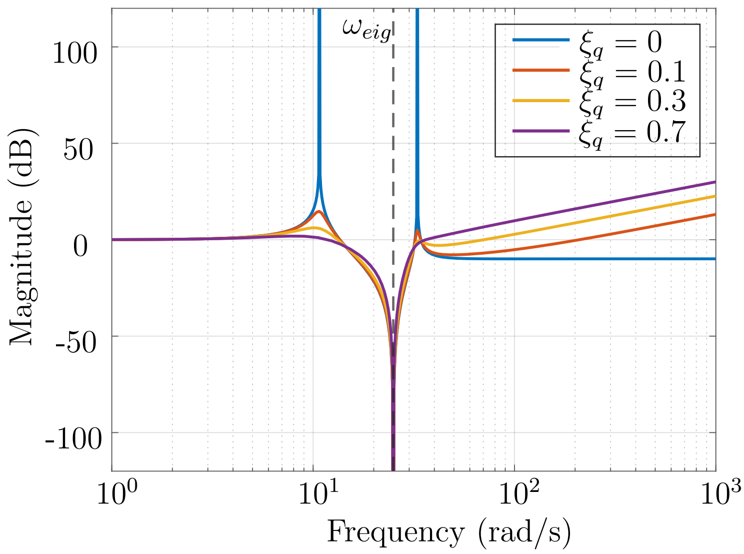

Figure 4.9: Bode plot of G_u with varying linkside damping factor ξ_q
$K = 374$ Nm/rad, $K_q = 200$ Nm/rad

increasing linkside damping factor ξ_q. The spikes appear at the poles of the transfer function G_u. When the poles match with the excitation frequency of the external disturbance, the peak control effort u_{peak} increases (especially for low ξ_q), which influences the optimal intrinsic stiffness value K^u_{opt}. The poles are calculated by solving the characteristic equation of the undamped system [21]. Rearranging the characteristic equation for the intrinsic stiffness K allows calculating the stiffness K_{spike}:

$$K_{spike} = \frac{B\,K_\mathrm{q}\,\omega_{ext}^2 - B\,M\,\omega_{ext}^4}{K_\mathrm{q} - B\,\omega_{ext}^2 - M\,\omega_{ext}^2} \tag{4.2}$$

K_{spike} represents the stiffness values corresponding to the spikes of the transfer function. Unlike K_{eig}, K_{spike} not only depends on ω_{ext} and B but also on M and K_q. Especially for lower linkside damping ξ_q, the peak amplitude of the control effort u_{peak} rises when the intrinsic stiffness is set to K_{spike}.

Fig. 4.10 shows the relationship between K_{spike} and K_q calculated using Eq. (4.2) for an excitation frequency of $\omega_{ext} = 2$ Hz with $A_1 = 1$ Nm. Fig. 4.11 displays u_{peak}

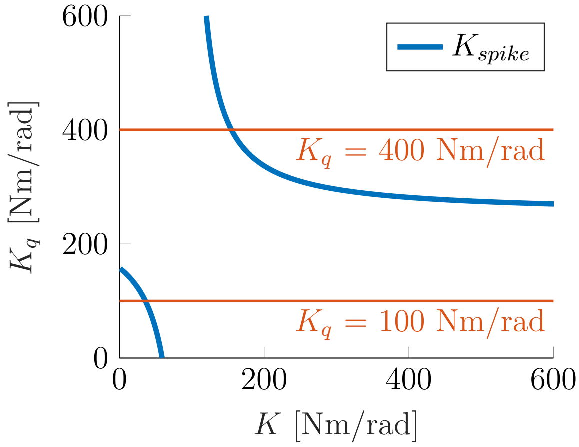

Figure 4.10: Stiffness values K_{spike} leading to peaks for $\omega_{ext} = 2$ Hz

over K for $K_q = 400$ Nm/rad (upper orange line in Fig. 4.10) and varying linkside damping factors. Here K_{spike} lies at 155 Nm/rad. As anticipated, decreasing the

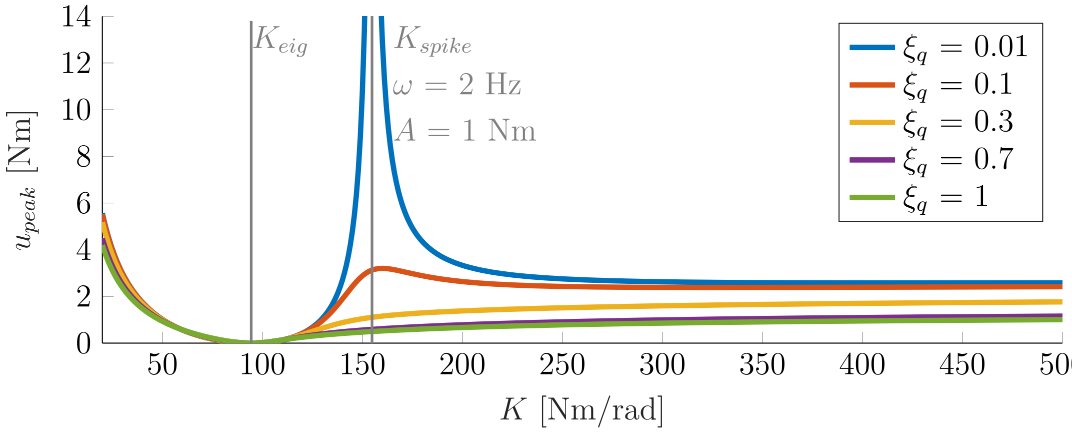

Figure 4.11: Damping variation for $\omega_{ext} = 2$ Hz, $K_q = 400$ Nm/rad

linkside damping results in a higher peak at K_{spike}. For $\xi_q > 0.3$, u_{peak} is not affected significantly by K_{spike} anymore. At K_{spike}, $\xi_q = 0.1$ results in an amplitude five times higher than that of $\xi_q = 0.7$. Additionally, a higher damping factor appears to lead to lower u_{peak} especially for intrinsic stiffness values greater than K_{eig} in this disturbance scenario. However, this trend does not hold true for other disturbances as Fig. 4.12 shows. It displays u_{peak} for the same damping factors but an excitation frequency $\omega_{ext} = 3$ Hz and $K_q = 100$ Nm/rad. Here, the opposite to the previous example is observed, with lower damping resulting in lower u_{peak}. Additional research is required to determine under which circumstances increasing the damping leads to higher/lower u_{peak}.

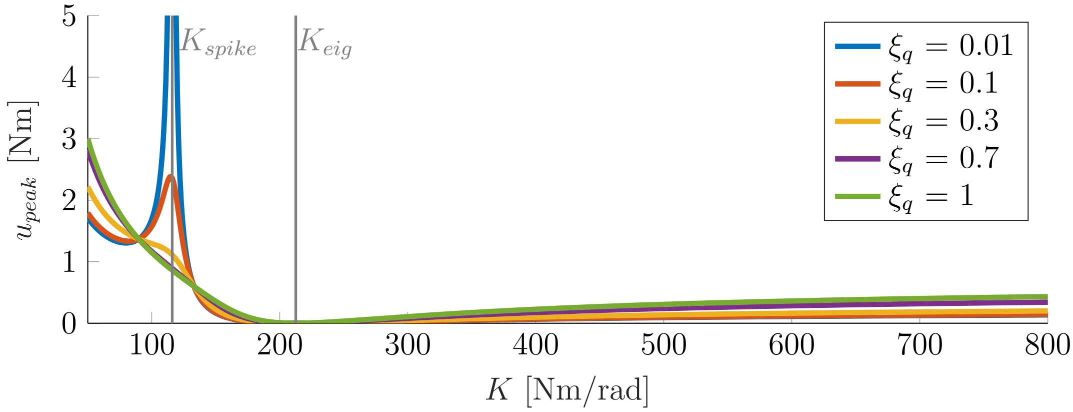

Figure 4.12: Damping variation for $\omega_{ext} = 3$ Hz, $K_q = 100$ Nm/rad

4.1.2 Experiments on minimization of power input

This section covers the minimization of the average power input $P_{input,\varnothing}$ while the link is under sinusoidal disturbance $\tau_{ext,osc}$ according to Problem 2.
To calculate $P_{input,\varnothing}$ (cf. Eq. (3.23)), the velocity of the motor coordinate $\dot{\theta}$ and the control effort u are derived via the transfer functions $G_{\dot{\theta}}$ and G_u (cf. Eq. (3.28) and Eq. (3.9)). The bode plots of both transfer functions are shown in Fig. 4.13 for $\xi_q = 0$ and Fig. 4.14 for $\xi_q = 0.7$.

$K = 374$ Nm/rad, $K_q = 200$ Nm/rad, $\xi_\eta = 0$

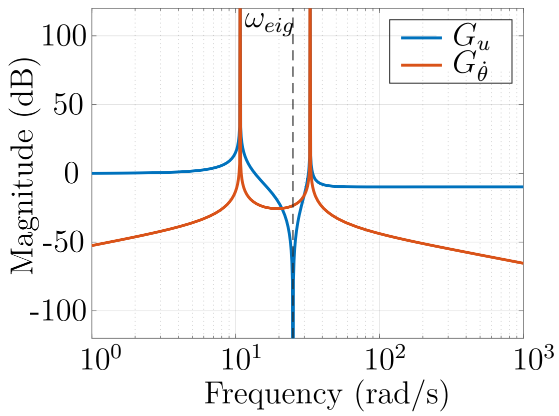

Figure 4.13: Bode plot of G_u and $G_{\dot{\theta}}$ $\xi_q = 0$

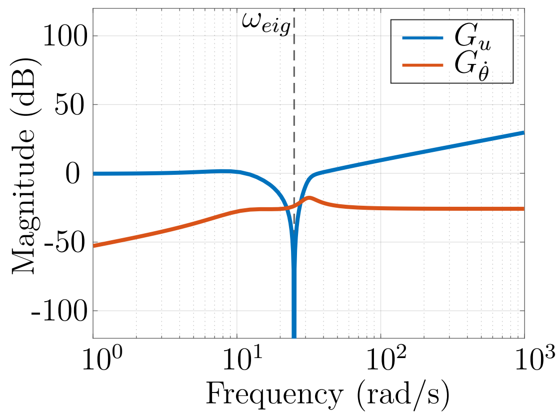

Figure 4.14: Bode plot of G_u and $G_{\dot{\theta}}$ $\xi_q = 0.7$

Both transfer functions G_u and $G_{\dot{\theta}}$ have the same positive spikes at their poles. Only G_u has a negative spike at the eigenfrequency ω_{eig}. When the excitation frequency of the disturbance matches with the poles it can result in a high average power input $P_{input,\varnothing}$, especially for low linkside damping ξ_q. When the linkside damping factor ξ_q is increased, the positive spikes of G_u and $G_{\dot{\theta}}$ are damped.
Fig. 4.15 shows $P_{input,\varnothing}$ over K and K_q for a single frequency disturbance with 2 Hz and an amplitude of 20 Nm. The z-axis is scaled logarithmically. As expected, $P_{input,\varnothing}$ is minimal for $K^P_{opt} = K_{eig} = 94.4$ Nm (green line in Fig. 4.15) regardless of K_q, since $\omega_{ext} = \omega_{eig}$ for this stiffness. The magnitude of $P_{input,\varnothing}$ ranges from 0 W to 16.05 W for an excitation amplitude of 20 Nm. The highest power input is reached for stiffness values at the lower intrinsic stiffness border of $K = 50$ Nm, which was the case for all performed experiments. This is due to the fact that

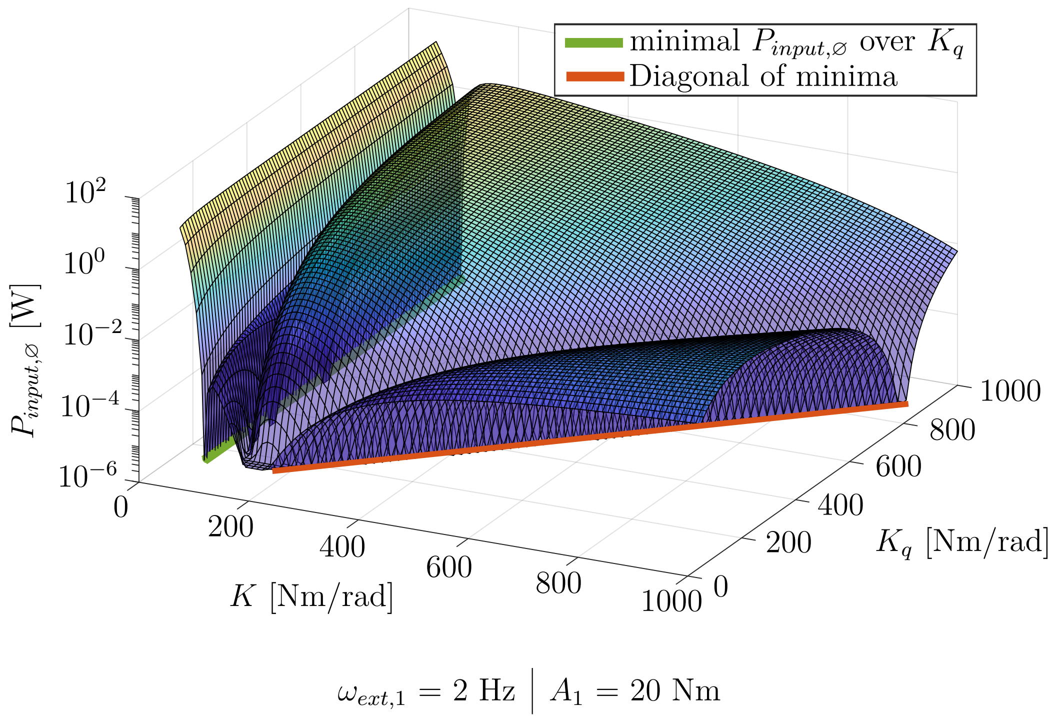

Figure 4.15: Average power input $P_{input,\varnothing}$ over K and K_q

for low stiffness values, ω_{eig} is smaller than ω_{ext} which means that ω_{ext} lies in the frequency range where $|G_{u,red}|$ rises with 20 dB/decade. This results in a rising magnitude amplification $|G_{u,red}|$ when the stiffness K is further decreased below K_{eig}.

Apart from the minima at K_{eig} there is another diagonal line of minima in the plot for $K > 200$ Nm where the average power input $P_{input,\varnothing}$ is low (red line in Fig. 4.15). On this diagonal, the average power input $P_{input,\varnothing}$ is smaller than 1×10^{-5} W, essentially zero. When analyzing the diagonal of multiple different excitations, it stands out that the slope of the diagonals is always 1, regardless of the external excitation. To describe this diagonal, a linear equation is used:

$$K_{q,diag} = K_{diag} + b \tag{4.3}$$

With changing parameters, the diagonal is shifted by b.

Fig. 4.16 shows the diagonal of the minima for different excitation frequencies between 1 Hz and 4 Hz with their respective b. It shows that b declines with rising

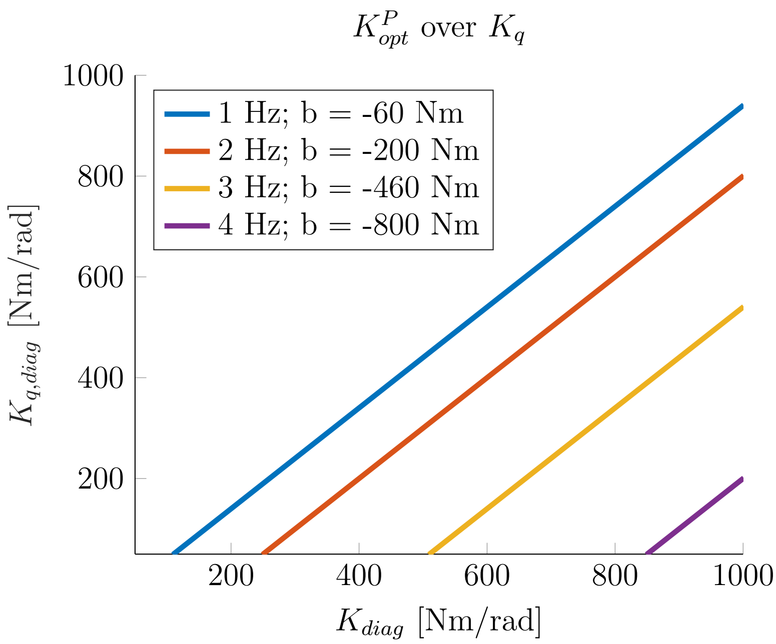

Figure 4.16: Minimal average power input $P_{input,\varnothing}$ lies on diagonal for varying ω_{ext}

excitation frequency. When K_{diag} is known for one value of $K_{q,diag}$, it is possible to calculate K_{diag} for any other K_q using Eq. (4.3).

Excitation with multiple frequency components

For external disturbances with multiple frequency components, the course of the minima run diagonally as well. Fig. 4.17 shows the plot of $P_{input,\varnothing}$ over K and K_q for an excitation with 1.5 Hz and 3 Hz. The green line representing the minimal average power input over K_q runs diagonally, however the diagonal starts only above a certain value of K_q. The reason for this are the spikes of the transfer functions G_u and $G_{\dot{\theta}}$ (cf. Fig. 4.13), which result in a higher average power input $P_{input,\varnothing}$ at certain stiffness values K_{spike}. The position of those peaks is derived from the poles of $G_u/G_{\dot{\theta}}$ and can be calculated with Eq. (4.2) as discussed in the last chapter. Although the spikes are low for a damping factor of $\xi_q = 0.7$, they still have an influence on the optimal intrinsic stiffness values $K_{opt}^P/K_{opt,glob}^P$.
To illustrate this, Fig. 4.18 shows the course of K_{opt}^P over K_q for varying damping factors with respect to the same disturbance as in the last example. The red and yellow lines represent the spikes in $P_{input,\varnothing}$ for the respective excitation frequencies

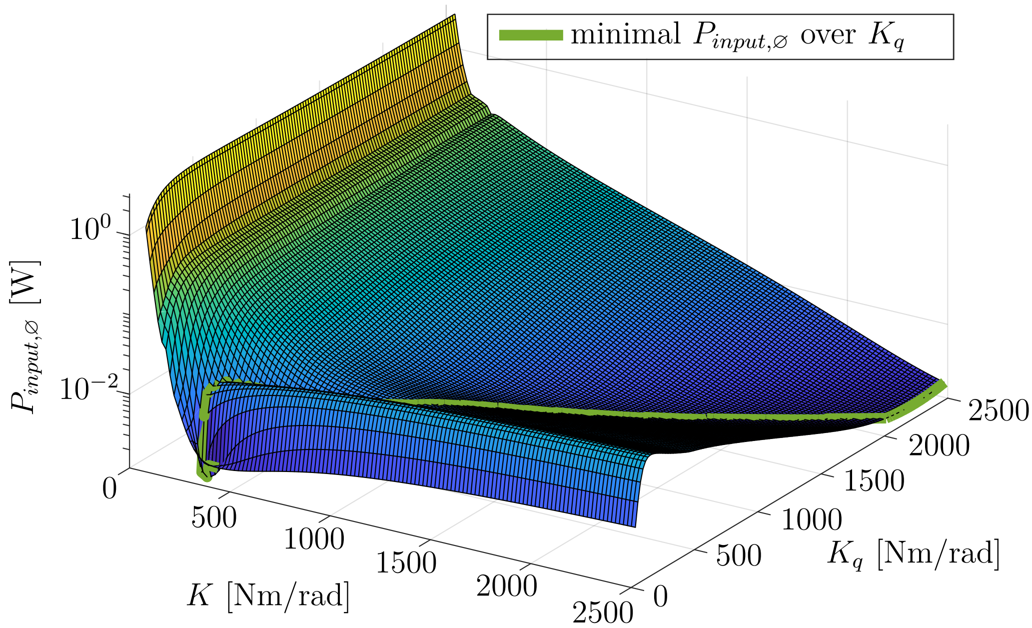

$$\begin{array}{r|l} \omega_{ext,1} = 1.5 \text{ Hz} & A_1 = 5 \text{ Nm} \\ \omega_{ext,2} = 3 \text{ Hz} & A_2 = 3 \text{ Nm} \end{array}$$

Figure 4.17: $P_{input,\varnothing}$ over K and K_q - diagonal minima

$\omega_{ext,1}$ and $\omega_{ext,2}$. Clearly, the diagonal behavior starts for stiffness values above the higher K_{spike}, regardless of the damping factor. The lower spike (red line) for $\omega_{ext} = 1.5$ Hz also influences the optimal stiffness value K^P_{opt}. For stiffness values below the higher K_{spike} (yellow line), no consistent behavior for the course of K^P_{opt} is found. In these cases, an optimization is needed to calculate $K^P_{opt}/K^P_{opt,glob}$.
Fig. 4.18 also shows the damping factor influencing the position of the diagonal: Increasing the damping factor decreases b. The slope of the diagonal remains constant at 1, regardless of the damping factor.

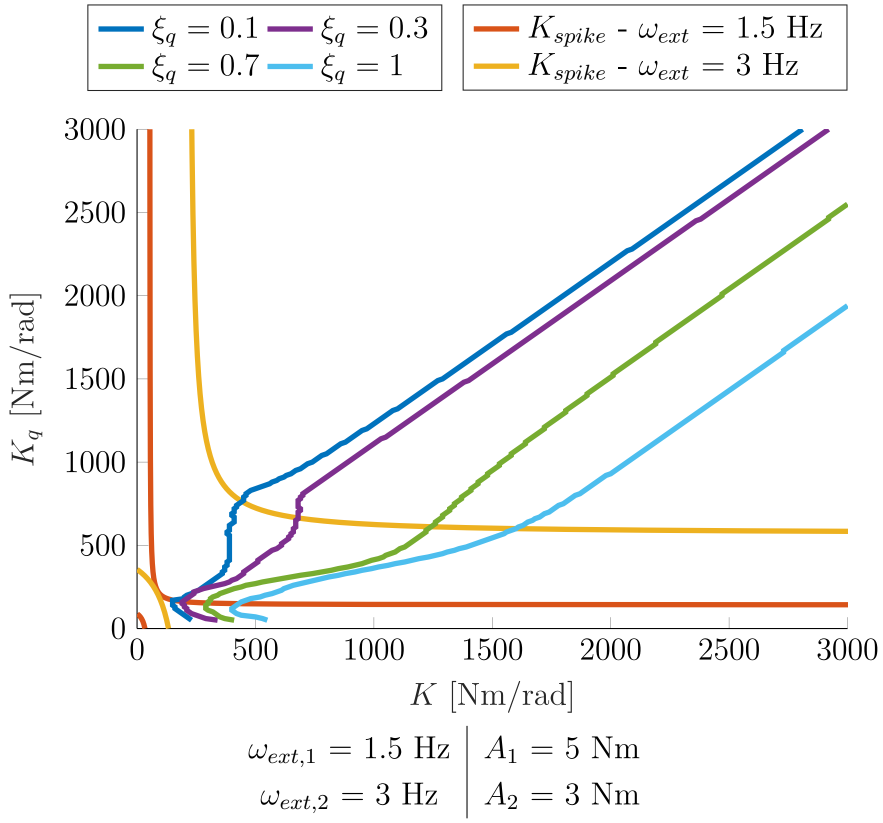

Figure 4.18: Influence of K_{spike} on diagonal for different damping factors ξ_q. The diagonal lines represent the course of K^P_{opt} over K_q

Analysis of power input vs power output

This section compares the power input and the power output through the power port $P_{ms} = \dot{\theta} \cdot u$ under different parameters (cf. Eq. (3.21)).
Fig. 4.19 shows the plot of the average power input $P_{input,\varnothing}$ (blue) and output $P_{output,\varnothing}$ (green) over the intrinsic stiffness K. The regarded external disturbance for this example is written below Fig. 4.19. Setting the intrinsic stiffness to the optimal stiffness calculated by solving Problem 2 $K^P_{opt} = 651$ Nm/rad leads to the minimal power input of 3.66 mW (see Fig. 4.20(b)). In the stiffness range of [50, 2000] Nm/rad, the power input varies between 3.66 mW and 2.4 W for this disturbance. The absolute power output varies between 254.44 mW and 2.68 W.
Fig. 4.20(a)-(c) illustrate the relationship between power input (red) and power output (blue) for the same external disturbance. The graph shows the power

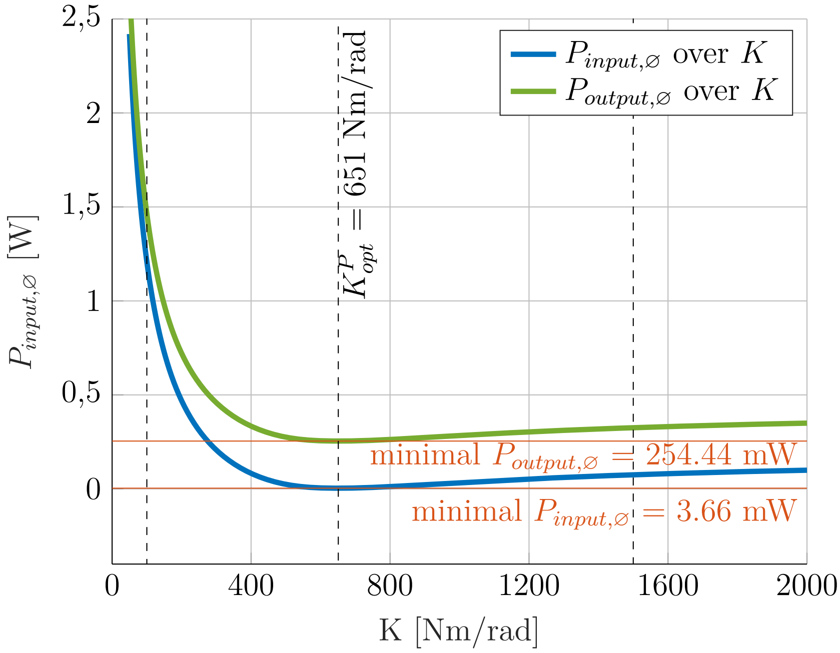

$\omega_{ext,1} = 0.5$ Hz	$A_1 = 10$ Nm
$\omega_{ext,2} = 1$ Hz	$A_2 = 10$ Nm

Figure 4.19: Comparison of average power input $P_{input,\varnothing}$ and output $P_{output,\varnothing}$ over K
$K_q = 600$ Nm/rad

transmitted through the powerport P_{ms} over time for three different stiffness values. The three considered stiffness values are highlighted by the dashed lines in Fig. 4.19. In Fig. 4.20(a)-(c) the values on the dashed lines show the respective values of $P_{input,\varnothing}$ and $P_{output,\varnothing}$. For the intrinsic stiffness $K = 100$ Nm/rad, both the power input and the power output are the highest compared to the other stiffness values. Additionally, the ratio between $P_{input,\varnothing}$ and $P_{output,\varnothing}$ is the highest. This ratio is calculated using Eq. (4.4) resulting in $R_{in,out} = 0.8$ for $K = 100$ Nm/rad.

$$R_{in,out} = \left| \frac{P_{input,\varnothing}}{P_{output,\varnothing}} \right| \tag{4.4}$$

Fig. 4.20(b) shows the power throughput for the optimal intrinsic stiffness of $K_{opt}^P = 651$ Nm/rad. Both $P_{input,\varnothing}$ and $P_{output,\varnothing}$ as well as $R_{in,out}$ are minimal at this stiffness setting. Multiple experiments conducted at different disturbance frequencies have shown that calculating the optimal intrinsic stiffness K_{opt}^P which

minimizes the power input also minimizes the absolute value of the power output $|P_{output,\varnothing}|$. This is also seen in this example. Additionally, for the optimal stiffness the power input-output ratio is always the lowest at K_{opt}^{P}, meaning that $P_{input,\varnothing} << P_{output,\varnothing}$. For the optimal intrinsic stiffness $K_{opt}^{u} = 651$ Nm/rad shown in Fig. 4.20(b), the ratio is 0.014.
Fig. 4.19 and Fig. 4.20(c) show that for $K > K_{opt}^{u}$, $P_{input,\varnothing}$, $P_{output,\varnothing}$ and $R_{in,out}$ rise again, but comparably slow. Fig. 4.19 also shows that the average power input is always greater than the power output for $\xi_q = 0.7$ meaning that $R_{in,out} < 1$ for all stiffness values K. For lower damping factors, the ratio $R_{in,out}$ increases. Without damping ($\xi_q = 0$), the average power input equals the average power output ($P_{input,\varnothing} = P_{output,\varnothing}$) meaning that the power input-output ratio $R_{in,out} = 1$.

In summary, Section 4.1.2 demonstrates that the optimal intrinsic stiffness K_{opt}^{P} with respect to an external disturbance can be calculated by solving Problem 2. Additionally, certain heuristics have been identified to aid in the selection of an intrinsic stiffness value K which leads to low average power input $P_{input,\varnothing}$ without optimization. However, it is questionable whether the influence of K_{opt}^{P} on the average power input $P_{input,\varnothing}$ justifies the use of the heuristics or the optimization, since the power input increases very little with changing intrinsic stiffness values, especially for $K > K_{opt}^{P}$.

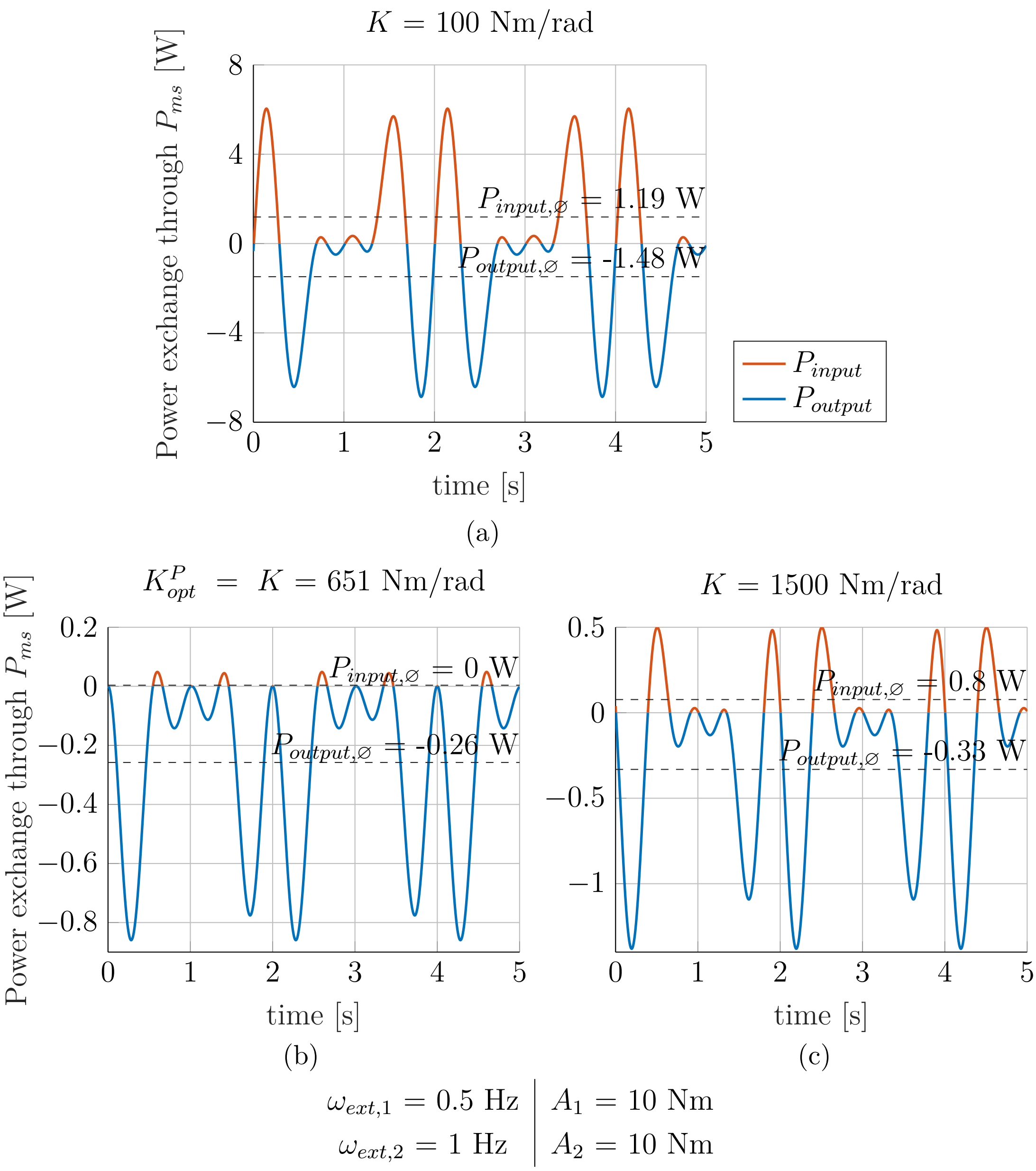

Figure 4.20: Power exchange through P_{ms} with varying intrinsic stiffness values K

4.2 Experiments with nonlinear elastic element

This section presents the results for simulations of the ESπ controller on a one DoF system with nonlinear stiffness characteristics. As for the linear case, minimization of the peak control effort u_{peak} and of the average power input $P_{input,\varnothing}$ by adjusting the intrinsic stiffness setting is addressed by solving Problem 3 and Problem 4. For the nonlinear case, a Simulink simulation is needed to derive u and $P_{input,\varnothing}$. This procedure is addressed in Section 3.2. For the following section, the motorside damping factor ξ_η is set to 0.3, because this factor proofed to be reliable for practical applications. As in the linear case, the linkside damping factor ξ_q is set to 0.7.

4.2.1 Minimization of the peak control effort for nonlinear VSAs

This section analyzes the impact of the intrinsic stiffness setting σ of an FSJ and of the controlled stiffness K_q on the peak control effort u_{peak}. For this purpose, several plots are analyzed to derive heuristics for the optimal intrinsic stiffness setting σ_{opt}. Also, Problem 3 is solved in order to calculate the optimal intrinsic stiffness settings $\sigma^u_{opt,glob}/\sigma^u_{opt}$ which are defined in Eqs. (3.36) and (3.37).
Figure 4.21 shows the surface plot of u_{peak} over varying intrinsic stiffness settings σ and controlled stiffness values K_q. The link is excited with an excitation frequency ω_{ext} of 1.5 Hz and an amplitude of 5 Nm. The peak amplitude of the control effort u_{peak} varies between 3 Nm and 6 Nm. The green line in the plot shows the minimal peak control effort $u_{peak,min}$ at its optimal stiffness setting σ^u_{opt} over K_q. σ^u_{opt} ranges from $\sigma = 0.2°$ for $K_q >$ 330 Nm to $\sigma = 1.6°$ for low K_q. This is different to the linear case, where the optimal stiffness K^u_{opt} was always constant for disturbances with one frequency component. For stiffness settings $\sigma < \sigma^u_{opt}$, the peak amplitude of the control effort u_{peak} increases more rapidly compared to stiffness settings $\sigma > \sigma^u_{opt}$. This trend is also observed for linear spring characteristics (refer to Section 4.1.1).
To evaluate the influence of the excitation frequency of the disturbance on the optimal stiffness setting σ^u_{opt}, Fig. 4.22 shows u_{peak} over σ for varying excitation frequencies between 1 Hz and 4 Hz. The amplitude of all excitations is set to

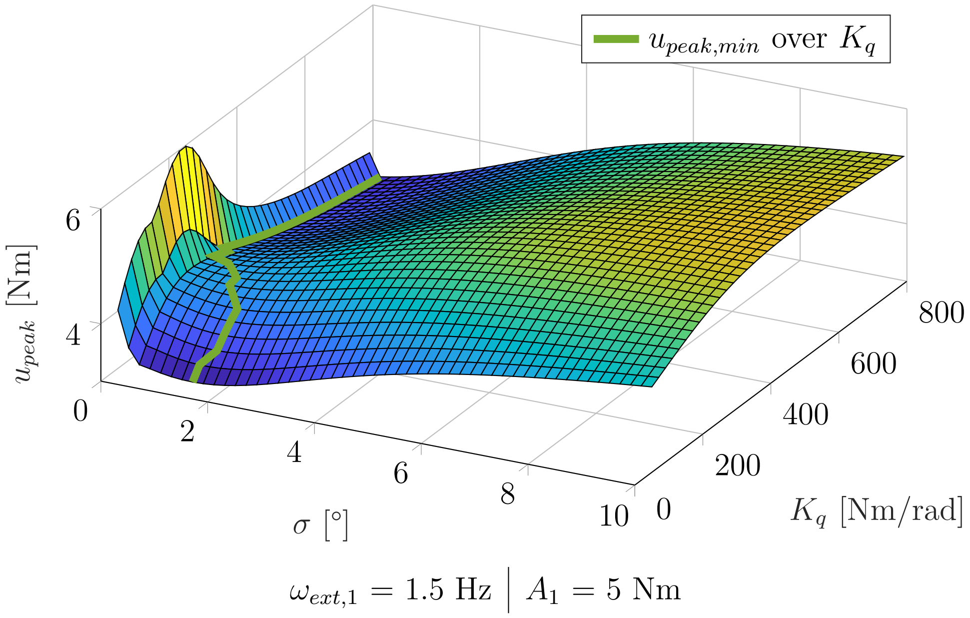

Figure 4.21: u_{peak} over K and K_q - nonlinear spring characteristics

5 Nm and the controlled stiffness is set to $K_q = 500$ Nm/rad. With increasing excitation frequencies, the minimal amplitude of the control effort lies at higher stiffness settings σ (σ^u_{opt} rises).

Fig. 4.22 shows that as the excitation frequency ω_{ext} increases, the value of u_{peak} is affected more by the choice of the stiffness setting σ. For instance, the value of u_{peak} varies by 66 Nm for $\omega_{ext} = 4$ Hz, whereas it only varies by 1 Nm for $\omega_{ext} = 1$ Hz. Additionally, Fig. 4.22 shows that the minimum peak amplitudes of the control effort $u_{peak,min}$ differ when changing the excitation frequency. The lowest amplitude of the control effort is reached at 3 Hz for $\sigma^u_{opt} = 4.9°$.

The plot also shows how u_{peak} rises rapidly for stiffness settings below the respective optimal stiffness settings σ^u_{opt} of the excitation frequencies.

For linear spring characteristics, the amplitude of the external disturbance A_i scales directly proportional with the peak amplitude of the control effort u_{peak}. For nonlinear stiffness values, this is not the case. Increasing the amplitude results in higher deflection of the spring ϕ which results in higher stiffness values (see Fig. 3.4). This influences the resulting control effort. To evaluate the impact of changing the amplitude on the control effort, Fig. 4.23 shows u_{peak} over σ for different excitation amplitudes A_i. The excitation frequency is set to 2 Hz and the controlled stiffness

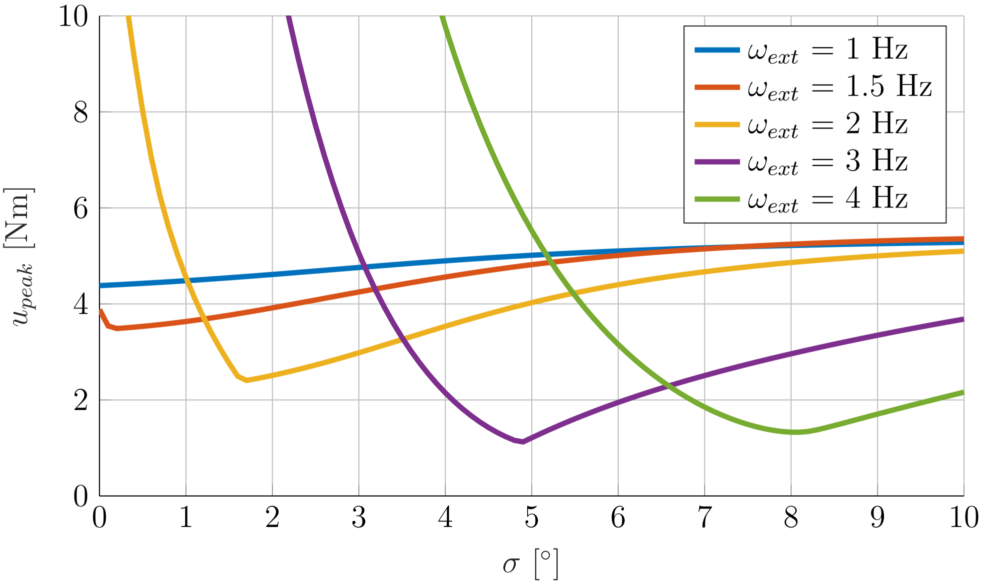

Figure 4.22: u_{peak} over σ for different excitation frequencies
$A_1 = 5$ Nm, $K_q = 500$ Nm/rad

K_q to 500 Nm/rad. The amplitudes A_i range from 1 Nm to 20 Nm. The control effort is normalized with respect to the amplitude of the excitation:

$$u_{peak,norm,i} = \frac{u_{peak,i}}{A_i}; \tag{4.5}$$

This way, the results are easier to compare. The red crosses mark the normalized minimal peak amplitude of the control effort $u_{peak,norm,min}$ for the respective amplitudes. The plot shows that increasing the amplitudes has an impact on the optimal stiffness setting σ^u_{opt}. σ^u_{opt} rises with the amplitude A_i of the external excitation. Also, for all amplitudes, $u_{peak,norm}$ convergences to 1 for high stiffness settings. This means, that for high stiffness settings σ, $u_{peak,i}$ equals the excitation amplitude A_i. For low amplitudes, $u_{peak,norm,min}$ is lower than for high amplitudes. For instance, $u_{peak,norm,min}$ is only 10 % of A_1 for $A_1 = 1$ Nm (blue line). For $A_{20} = 20$ Nm, $u_{peak,norm,min}$ is almost exactly equal to its excitation amplitude $A_{20} = 20$ Nm. This means that optimizing the stiffness setting to calculate σ^u_{opt} for high amplitudes A_i brings no huge benefit compared to the highest stiffness setting ($\sigma = 10°$). On the other hand, when the stiffness is set smaller than σ^u_{opt}, $u_{peak,norm}$ gets higher than the excitation amplitude quickly for high amplitudes. For lower amplitudes,

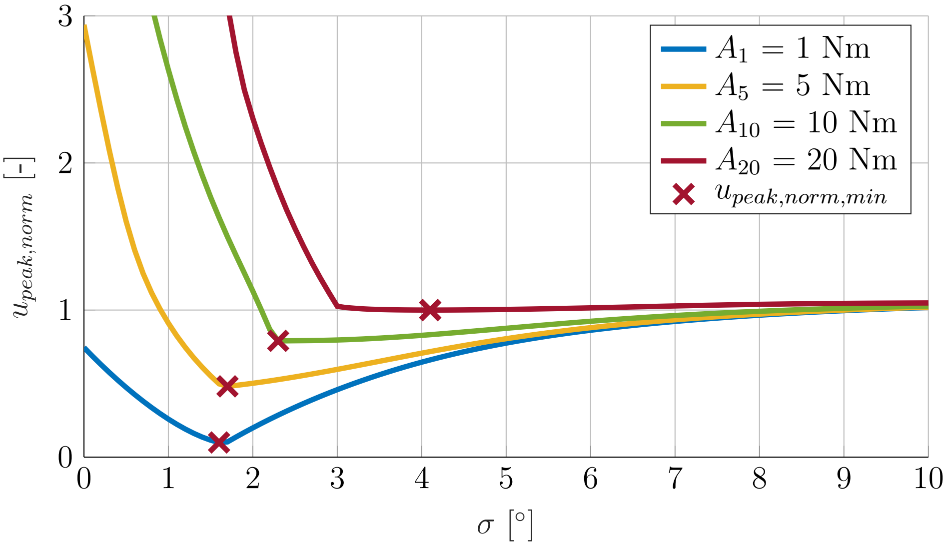

Figure 4.23: Variation of excitation amplitudes
$\omega_{ext} = 2$ Hz, $K_q = 500$ Nm/rad

optimizing the stiffness setting is more beneficial. For instance, at $A_5 = 5$ Nm (yellow line), $u_{peak,norm,min}$ at $\sigma^u_{opt} = 1.7°$ is only 48 % of A_5.

Comparison between linear and nonlinear spring characteristics

This section compares the peak control effort of the nonlinear system calculated in Problem 3 with the one of linear spring systems calculated in Problem 1. It discusses the transferability of results from the linear system to the nonlinear system. Understanding the limits of transferability is advantageous because optimizing the linear system requires less computational effort, potentially enabling real-time optimization.

The comparison between the intrinsic stiffness K of a linear system and the stiffness setting of an FSJ is not straight forward since the stiffness setting of the latter is defined by the angle σ. In order to perform a comparison between the two systems, correlating stiffness values $K_{cor,\sigma}$ can be assigned to the stiffness settings σ. One possibility, which is used in the following, is to assign the stiffness $\kappa_\sigma(\phi = 0)$ of the FSJ at a link deflection of $\phi = 0$ to the corresponding values of σ:

$$\sigma \mathrel{\hat{=}} K_{cor,\sigma} = \kappa_\sigma(\phi = 0) \tag{4.6}$$

The stiffness settings σ with their corresponding stiffness values $K_{cor,\sigma}$ are shown in Fig. 4.24.

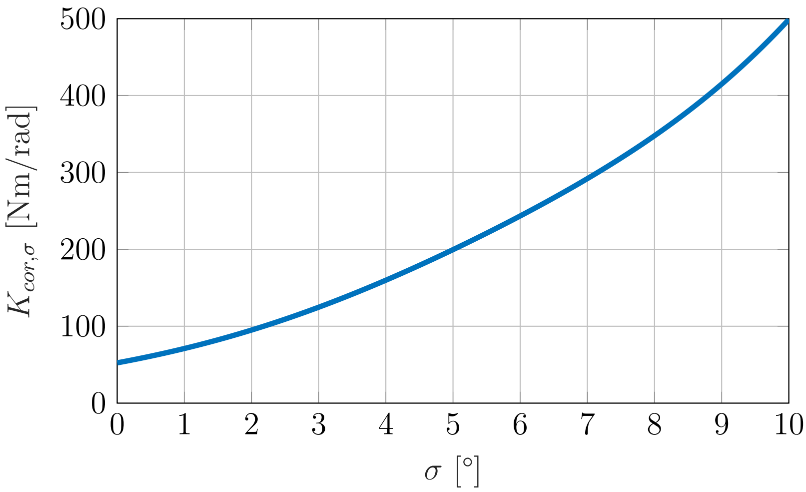

Figure 4.24: FSJ stiffness setting σ with its corresponding stiffness values $K_{cor,\sigma}$

Initially, the comparison is carried out for disturbances with one single frequency. Figure 4.25 shows the comparison between the linear and nonlinear case for an excitation with a frequency ω_{ext} of 2 Hz and an amplitude of 5 Nm. The plot

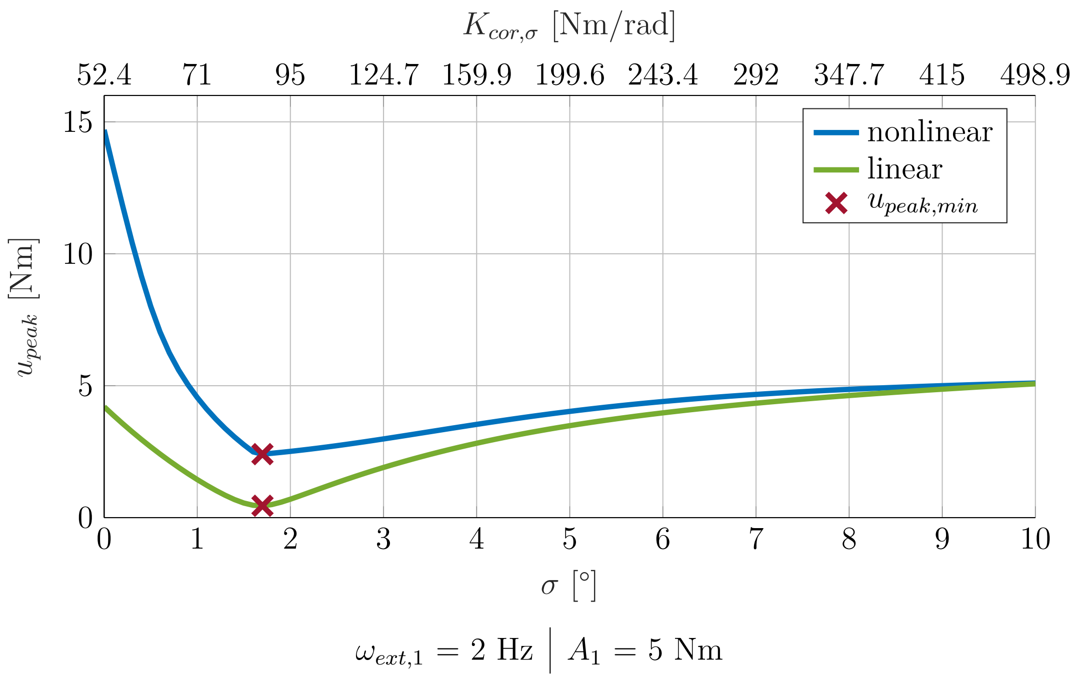

Figure 4.25: Comparison between linear and nonlinear spring characteristics
$K_q = 500$ Nm/rad

has two different x-axes. The lower axis shows the stiffness setting σ of the FSJ, with the corresponding stiffness values shown on the upper axis. The upper axis is nonlinear, since the correlation of σ and $K_{cor,\sigma}$ is also nonlinear (see Fig. 4.24). The plot shows the peak amplitude of the control effort u_{peak} of the nonlinear FSJ in blue and that of the linear joint in green for different intrinsic stiffness settings σ. The red crosses mark the respective minimum peak amplitudes $u_{peak,min}$.

The general course of both curves is similar, however as σ decreases, they diverge more. This is because for lower stiffness settings σ, the joint deflection ϕ is higher, which results in the nonlinear effects of the FSJ becoming more significant. For high stiffness settings, the joint is deflected less so the stiffness also changes less which is more similar to the linear case. That is why the resulting peak amplitude of the control effort u_{peak} for the linear and nonlinear case converge with rising stiffness settings.

Furthermore, the peak amplitude of the control effort u_{peak} of the nonlinear system is higher than that of the linear system over the full stiffness range σ. This phenomenon is observed for the majority of simulated disturbances with a single frequency:

$$u_{peak,nonlinear} \gtrsim u_{peak,linear} \; \forall \; \sigma \tag{4.7}$$

Only for very low amplitudes $A_i \lesssim 3$ Nm some experiments showed that the nonlinear elastic element led to slightly lower peak amplitudes u_{peak} like shown in Fig. 4.26. In this example, both minima $u_{peak,min}$ lie at $\sigma^u_{opt} \approx 1.7° \mathrel{\hat{=}} K^u_{cor,\sigma} = 87.2$ Nm. However, the amplitude analysis of the last section (Fig. 4.23) shows that changing the amplitude changes the optimal stiffness setting σ^u_{opt} for nonlinear elastic elements. The optimal linear intrinsic stiffness K^u_{opt} on the other hand stays constant when changing the excitation amplitude. This shows that the value of K^u_{opt} of the linear system does not necessarily equal the corresponding optimal value σ^u_{opt} of the nonlinear system. Generally experiments showed that the optimal stiffness setting $\sigma^u_{opt} \mathrel{\hat{=}} K^u_{cor,\sigma,opt}$ of the nonlinear system is approximately equal or higher than the optimal stiffness K^u_{opt} of the linear system for excitations with one frequency component:

$$\sigma^u_{opt} \mathrel{\hat{=}} K^u_{cor,\sigma,opt} \gtrsim K^u_{opt} \; \forall \; A_i \tag{4.8}$$

When the amplitude of the disturbance is further decreased, the nonlinear effects decrease because the joint deflection ϕ decreases. Consequently, the nonlinear system approaches the linear system. This is shown in Fig. 4.26 where the external disturbance has an amplitude $A_1 = 1$ Nm. Both curves are now similar to each other, regardless of the stiffness setting σ. The minimal peak amplitudes $u_{peak,min}$ are also similar.

The previous results apply on disturbances with a single frequency. The following section discusses if they are applicable to external disturbances with multiple frequency components. Fig. 4.27 shows the peak amplitude of the control effort u_{peak} over σ for an excitation with 1.2 Hz and 3 Hz and an amplitude of 5 Nm and 1 Nm respectively. In contrast to the single frequency excitation, the peak amplitude u_{peak} of the nonlinear case is smaller than that of the linear case for stiffness values $\sigma > 6°$. Although most experiments have shown that the linear system leads to lower peak amplitudes, the statement made in Eq. (4.7) does not generally hold for excitations with multiple frequency components.

For this example, the optimal intrinsic stiffness setting σ^u_{opt} of the nonlinear system is $\sigma^u_{opt} = 3.7° \mathrel{\hat{=}} K^u_{cor,\sigma,opt} = 148.8$ Nm, while the optimal stiffness for the linear

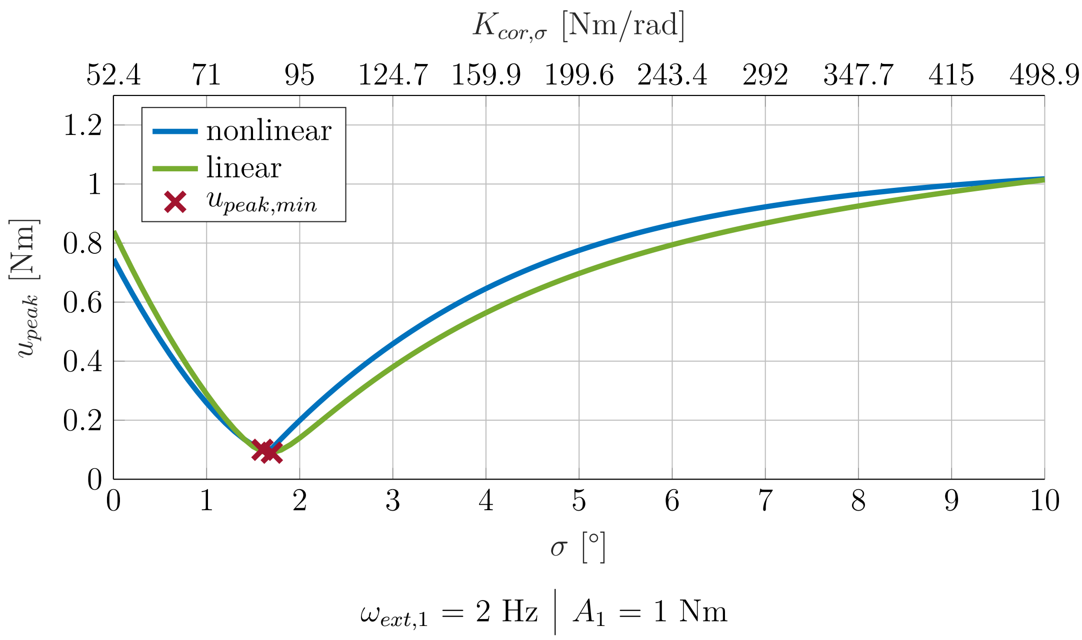

Figure 4.26: Comparison between nonlinear and linear system for low excitation amplitude
$K_q = 500$ Nm/rad

case is higher with $K^u_{opt} = 171.3$ Nm. Therefore, Eq. (4.8) also does not hold for excitations with multiple frequencies.
The results for multiple frequency disturbance show that the heuristics of the linear case are not transferable to the nonlinear case. To calculate the optimal intrinsic stiffness setting for those disturbances, Problem 3 needs to be solved

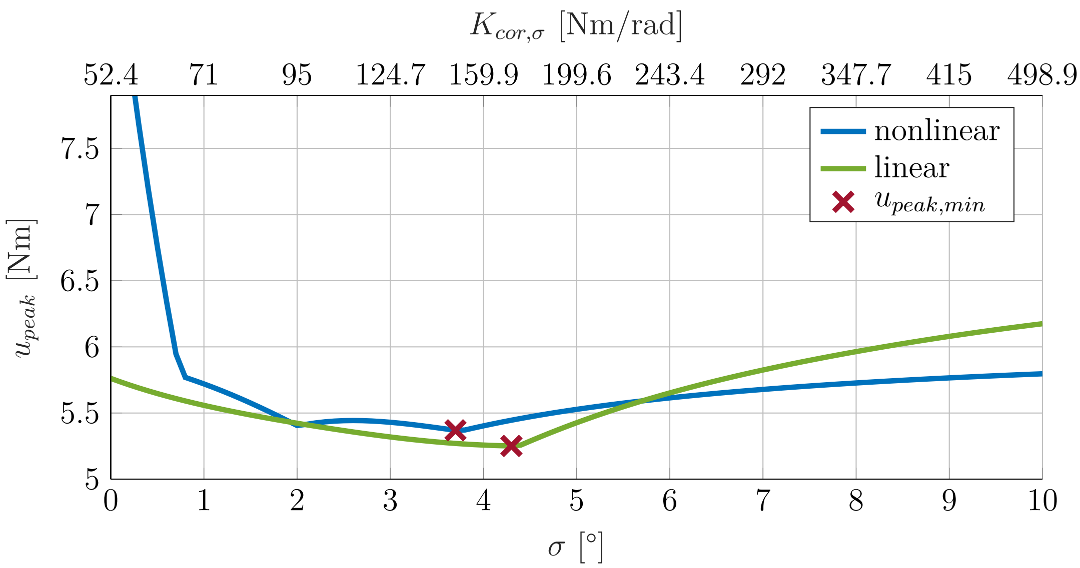

$\omega_{ext,1} = 1.2$ Hz | $A_1 = 5$ Nm
$\omega_{ext,2} = 3$ Hz | $A_2 = 1$ Nm

Figure 4.27: Comparison between linear and nonlinear system for disturbances with multiple excitation frequencies for $K_q = 200$ Nm/rad

4.2.2 Minimization of power input for nonlinear VSAs

This section covers the results of solving Problem 4. Solving Problem 4 calculates the optimal intrinsic stiffness settings $\sigma^P_{opt,glob}/\sigma^P_{opt}$ (defined in Eq. (3.38) and (3.39)) which minimize the average power input $P_{input,\varnothing}$ of the motor while the link is subjected to the disturbance $\tau_{ext,osc}$. To analyze the optimization results, several plots are shown.

Figure 4.28 shows the average power input $P_{input,\varnothing}$ over the intrinsic stiffness setting σ for $K_q = 500$ Nm/rad and varying excitation frequencies ω_{ext} between 1 Hz and 4 Hz. The amplitudes A_i of all excitations are set to 20 Nm. For all excitation frequencies except $\omega_{ext} = 3$ Hz, the optimal intrinsic stiffness setting σ^P_{opt} leading to minimal $P_{input,\varnothing}$ lies at the highest intrinsic stiffness setting $\sigma_{max} = 10°$. For all curves, $P_{input,\varnothing}$ rises quickly below some stiffness value, especially for higher excitation frequencies. At $\sigma^P_{opt} = 10°$, all excitations end up at a fairly low average power input $P_{input,\varnothing} < 0.2$ W. The highest average power input is reached at the lowest stiffness setting of $\sigma_{min} = 0°$. For the higher excitation frequencies

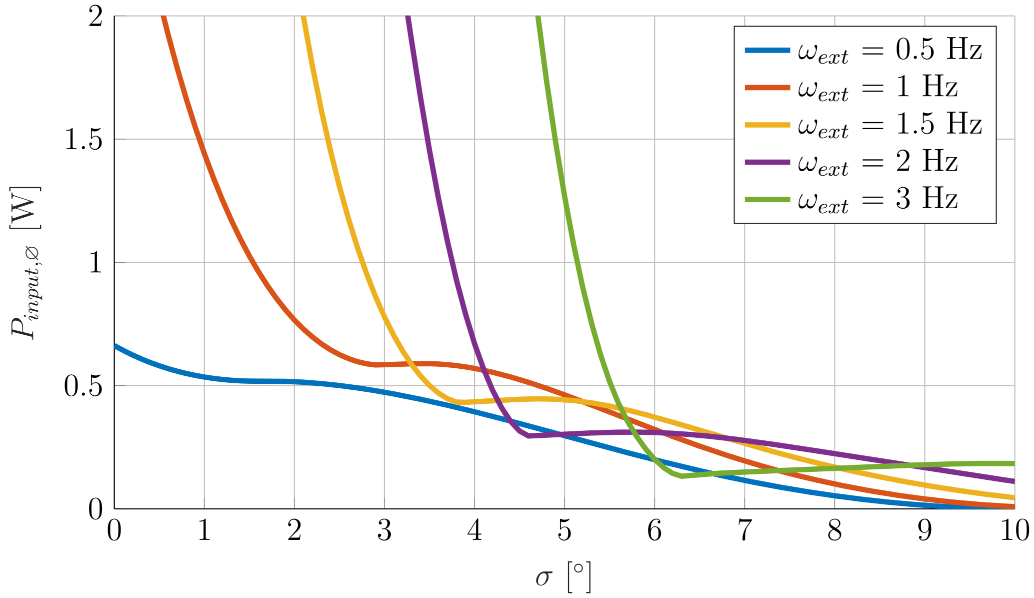

Figure 4.28: $P_{input,\varnothing}$ over σ for different excitation frequencies
$A_1 = 20$ Nm, $K_q = 500$ Nm/rad

$\omega_{ext} \geq 1.5$ Hz, the average power input $P_{input,\varnothing}$ is 45 W or higher at σ_{min}. However, it is not realistic to expect disturbances with such high frequencies in combination with high amplitudes (20 Nm for this example) in practical situations.

Next, the impact of varying the amplitude on $P_{input,\varnothing}$ is addressed. Figure 4.29 shows $P_{input,\varnothing}$ for an excitation frequency of $\omega_{ext} = 2$ Hz and amplitudes A_i between 1 Nm and 20 Nm. The controlled stiffness K_q is set to 500 Nm/rad. As in the previous case, the optimal intrinsic stiffness σ^P_{opt} lies at $\sigma_{max} = 10°$ for all amplitudes. Also, all curves have a local minimum at different intrinsic stiffness values σ. For stiffness settings which are lower than that of the local minima, the $P_{input,\varnothing}$ rises quickly. The variation of $P_{input,\varnothing}$ over σ rises with rising excitation amplitude.

Lastly, the power input and power output through the powerport P_{ms} defined in Eq. (3.21) is analyzed. Figure 4.30 illustrates the power input in red and the power output in blue over 2 seconds. The dotted lines mark the average power input $P_{input,\varnothing}$ and output $P_{output,\varnothing}$. The regarded disturbance parameters are written in the table below Figure 4.30. The intrinsic stiffness setting leading to this power-throughput is the optimal intrinsic stiffness setting σ^P_{opt} calculated by solving Problem 4. Like also seen in the linear case (cf. Section 4.1.2 - Analysis of power

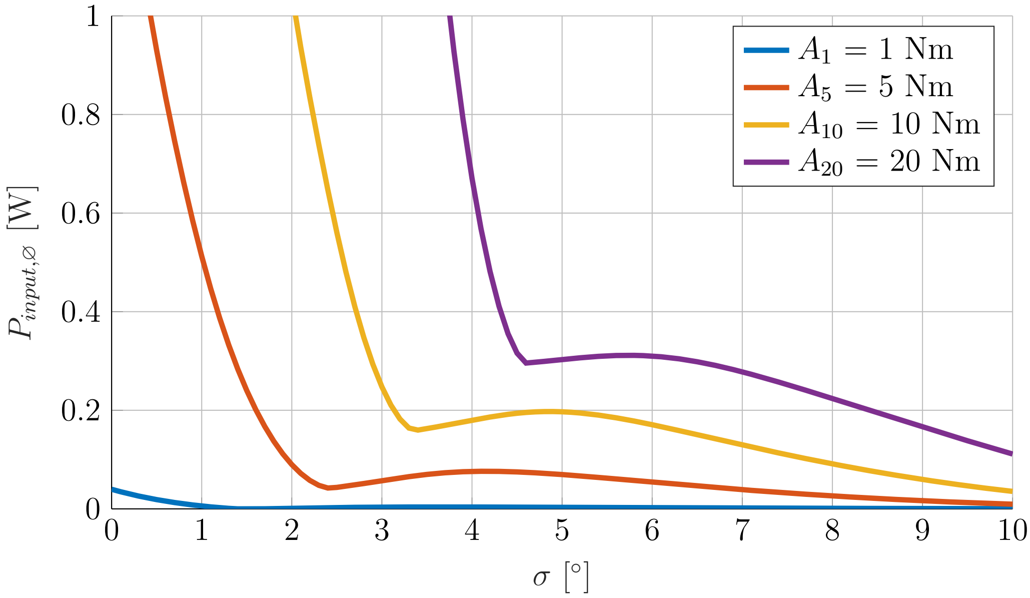

Figure 4.29: $P_{input,\varnothing}$ over σ for different excitation amplitudes A_i
$\omega_{ext} = 2$ Hz, $K_q = 500$ Nm/rad

input vs power output) the average power input $P_{input,\varnothing}$ is always smaller than the average power output $P_{output,\varnothing}$ if the linkside damping factor $\xi_q > 0$. Also, the ratio $R_{in,out}$ between $P_{input,\varnothing}$ and $P_{output,\varnothing}$ defined in Eq. (4.4) is the lowest at σ^P_{opt}. Unlike in the linear case, the power output is not minimal at σ^P_{opt}.
After performing multiple experiments for different external disturbances, the results show that for the majority of the disturbances, the highest stiffness setting σ_{max} of the FSJ leads to the minimal average power input ($\sigma^P_{opt} = \sigma_{max}$). This is why it is questionable whether the effort of performing the optimization of the intrinsic stiffness setting σ (cf. Problem 4) is worthwhile. In disturbance scenarios where σ^P_{opt} does not equal the maximum stiffness setting σ_{max}, the differences of $P_{input,\varnothing}$ at σ^P_{opt} and $P_{input,\varnothing}$ at σ_{max} do not prove to be significant in the performed experiments. This also shows the low impact of solving the optimization problem presented in Problem 4.

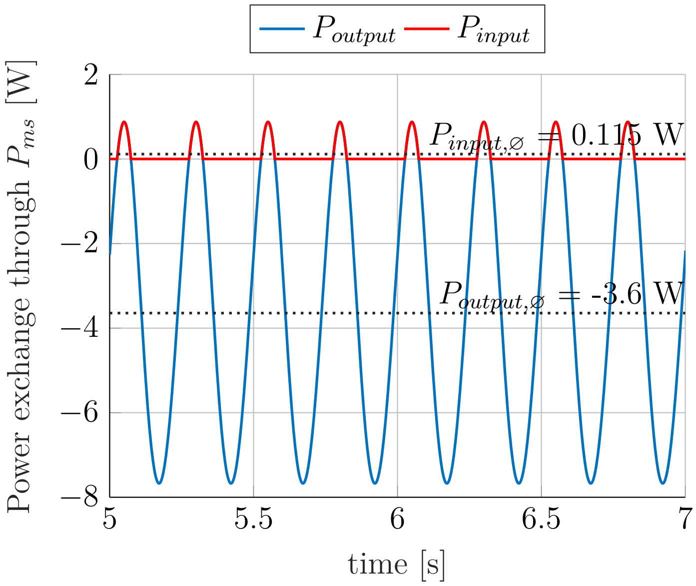

$\omega_{ext,1} = 0.2$ Hz | $A_1 = 20$ Nm

Figure 4.30: Power exchange through P_{ms}
$K_q = 600$ Nm/rad, $\sigma = 10°$

4.3 Conclusion

The following summarizes the results from Chapter 4. All sections cover the optimization of the intrinsic stiffness setting K/σ with respect to different objective functions while the system is under sinusoidal disturbance with a singular or multiple frequencies. Several optimization problems are formulated which minimize the peak control effort u_{peak} or the average power input $P_{input,\varnothing}$. They are summarized in Table 3.1

First, the analysis of the linear case is addressed. For a sinusoidal disturbance with a single frequency the experiments show that the intrinsic stiffness K can be set to K_{eig} in order to match the eigenfrequency of the system with the disturbance frequency in order to minimize the control effort. If the disturbance frequency is not known, it is more promising to set the intrinsic stiffness K to the highest setting to ensure a low control effort. The experiments show that a low controlled stiffness K_q mostly leads to lower control effort than higher controlled stiffness values. The applicability of this finding is limited since the controlled stiffness

usually cannot be chosen arbitrarily.
For disturbances with multiple frequencies in the linear case, the control effort can be minimized by solving an optimization problem (cf. Problem 1). The experiments show that the optimal intrinsic stiffness K^u_{opt} always lies in between the stiffness values $K_{eig,i}$ of the individual excitation frequencies. This enables the enhancement of the optimization algorithm by reducing the number of starting points (see Section 4.1.1 - Efficient solution of optimization problem). If no optimization is performed, setting the intrinsic stiffness to the value K_{eig} which is corresponding to the highest excitation frequency is expected to lead to a low control effort, provided that the amplitudes of the individual excitations are the same. If the amplitude of an excitation frequency is higher than that of the other excitation frequencies, the optimal intrinsic stiffness value K^u_{opt} shifts in the direction of the respective K_{eig}.
The next section covered the minimization of the power input of the motor in the linear case for the disturbance with a single frequency. Analog to the minimization of the control effort, setting the intrinsic stiffness to K_{eig} leads to the lowest power input.
The optimal intrinsic stiffness K^P_{opt} which reduces the average power input of the motor $P_{input,\varnothing}$ can be calculated by solving an optimization problem (Problem 2). If no optimization is performed, some heuristics can serve as a hint on how to set the intrinsic stiffness: For excitations with multiple frequencies, K_{eig} cannot be used as an orientation to set the optimal intrinsic stiffness. However, the analysis of plots shows that above a certain controlled stiffness K_q, the optimal stiffness values lie on a diagonal defined by $K_{q,diag} = K_{diag} + b$. Under certain circumstances, this allows the calculation of the optimal intrinsic stiffness K^P_{opt} (see Section 4.1.2). Finally, the experiments show that the minimization of the power input also leads to minimal power output.
For VSAs with a nonlinear elastic element, two more optimization problems which minimize the peak control effort u_{peak} and the average power input $P_{input,\varnothing}$ are formulated (cf. Problem 3 and 4). For solving the optimization problems of the nonlinear case, performing Simulink simulations is needed. For disturbance with a single frequency, some characteristics are identified for setting the intrinsic stiffness in order to minimize the peak control effort u_{peak} without performing an optimization:

- The optimal intrinsic stiffness setting σ^u_{opt} rises with the excitation frequency

ω_{ext}.

- The optimal intrinsic stiffness setting σ^u_{opt} rises the with excitation amplitude A_i.
- The lower the amplitude of the disturbance, the higher the benefit of optimization. For high amplitudes the optimized stiffness setting σ^u_{opt} does not reduce the peak control effort u_{peak} significantly compared to the highest stiffness setting.
- The optimal intrinsic stiffness setting σ^u_{opt} in the nonlinear case leads to higher minimal peak control effort $u_{peak,min}$ than the optimal intrinsic stiffness K^u_{opt} in the linear case for equal external disturbances.

These characteristics did not prove to be applicable for disturbances with multiple frequencies. In this case solving Problem 3 is needed to derive the optimal intrinsic stiffness setting σ^u_{opt}.

Finally, the minimization of the power input for the nonlinear case is analyzed. Even though σ^P_{opt} can be calculated by solving Problem 4, it is questionable whether the optimization results justify the effort of performing an optimization. For the majority of the disturbance scenarios, the highest possible stiffness setting σ_{max} leads to the minimal average power input $P_{input,\varnothing}$ meaning that $\sigma^P_{opt} = \sigma_{max}$.

5 Discussion and outlook

This thesis analyzes the impact of the adjustable intrinsic stiffness of VSAs on the control effort and the power input of the motor during external disturbances. The ESπ control concept presented in [16] which is used for the control of VSAs serves as the basis of the analyses performed in this thesis. The focus lies on sinusoidal disturbances with single and multiple frequencies. The analysis covers VSAs with both linear and nonlinear spring characteristics.

For the linear case, transfer functions are derived that allow the calculation of the control effort and the power input resulting from the disturbance. Additionally, optimization problems are formulated to determine the intrinsic stiffness which minimizes the control effort or power input under disturbance using the derived transfer functions. The optimization is improved for efficiency, which may enable real-time optimization for linear VSAs. However, this needs to be investigated further. For applications where the disturbances cannot be measured or no optimization is feasible, heuristics are derived which help choosing the intrinsic stiffness setting in those situations.

For VSAs with nonlinear spring characteristics, no analysis via transfer functions is possible. Thus, a Simulink model of a single DoF VSA is created, based on the FSJ used in the DLR David robot. The Simulink model is used for another optimization problem in order to find the optimal intrinsic stiffness setting which minimize the control effort or the power input. Optimizing the stiffness setting via the Simulink model is computationally expensive, which is problematic for real time applications. Consequently, more heuristics are derived, which help choosing the intrinsic stiffness of a VSA with respect to external disturbances.

In general, it can be stated that the adjustability of the intrinsic stiffness allows for a reduction in control effort when the VSA is under disturbance. The optimal intrinsic stiffness, which results in minimal control effort, is strongly dependent on the external disturbance and other control parameters of the ESπ controller. Therefore, it is necessary to measure the external disturbances and perform an optimization to find the optimal intrinsic stiffness value.

Although adjusting the optimal intrinsic stiffness has potential to minimize the control effort, its impact on the power input of the motor is comparably low. The reason for this is that the ESπ control concept is designed to change the original system dynamics to a minimal extent, i.e. that the controller introduces as little energy as possible into the system [1].

This thesis demonstrates the potential of using the adjustability of the intrinsic stiffness of VSAs to minimize control effort in disturbance scenarios. However, further research is necessary. While this thesis concentrated on sinusoidal disturbances, it may be worthwhile to explore other disturbance scenarios such as collisions. Furthermore, additional research could explore the effect of intrinsic stiffness on control effort in tracking scenarios.

References

[1] Manuel Keppler, Dominic Lakatos, Christian Ott, and Alin Albu-Schäffer. Elastic structure preserving (esp) control for compliantly actuated robots. *IEEE Transactions on Robotics*, 34(2):317–335, 2018. doi: 10.1109/TRO.2017.2776314.

[2] B. Vanderborght, A. Albu-Schaeffer, A. Bicchi, E. Burdet, D.G. Caldwell, R. Carloni, M. Catalano, O. Eiberger, W. Friedl, G. Ganesh, M. Garabini, M. Grebenstein, G. Grioli, S. Haddadin, H. Hoppner, A. Jafari, M. Laffranchi, D. Lefeber, F. Petit, S. Stramigioli, N. Tsagarakis, M. Van Damme, R. Van Ham, L.C. Visser, and S. Wolf. Variable impedance actuators: A review. *Robotics and Autonomous Systems*, 61(12):1601–1614, 2013. ISSN 0921-8890. doi: https://doi.org/10.1016/j.robot.2013.06.009. URL https://www.sciencedirect.com/science/article/pii/S0921889013001188.

[3] Manolo Garabini, Andrea Passaglia, Felipe Belo, Paolo Salaris, and Antonio Bicchi. Optimality principles in variable stiffness control: The vsa hammer. In *2011 IEEE/RSJ International Conference on Intelligent Robots and Systems*, pages 3770–3775, 2011. doi: 10.1109/IROS.2011.6094870.

[4] Manolo Garabini, Andrea Passaglia, Felipe Belo, Paolo Salaris, and Antonio Bicchi. Optimality principles in stiffness control: The vsa kick. In *2012 IEEE International Conference on Robotics and Automation*, pages 3341–3346, 2012. doi: 10.1109/ICRA.2012.6225176.

[5] J. Yamaguchi, S. Inoue, D. Nishino, and A. Takanishi. Development of a bipedal humanoid robot having antagonistic driven joints and three dof trunk. In *Proceedings. 1998 IEEE/RSJ International Conference on Intelligent*

Robots and Systems. Innovations in Theory, Practice and Applications (Cat. No.98CH36190), volume 1, pages 96–101 vol.1, 1998. doi: 10.1109/IROS.1998.724603.

[6] Bram Vanderborght, Björn Verrelst, Ronald Van Ham, Michaël Van Damme, Dirk Lefeber, Bruno Meira Y Duran, and Pieter Beyl. Exploiting natural dynamics to reduce energy consumption by controlling the compliance of soft actuators. *The International Journal of Robotics Research*, 25(4):343–358, 2006. doi: 10.1177/0278364906064566. URL https://doi.org/10.1177/0278364906064566.

[7] G. Tonietti, R. Schiavi, and A. Bicchi. Design and control of a variable stiffness actuator for safe and fast physical human/robot interaction. In *Proceedings of the 2005 IEEE International Conference on Robotics and Automation*, pages 526–531, 2005. doi: 10.1109/ROBOT.2005.1570172.

[8] Oliver Eiberger, Sami Haddadin, Michael Weis, Alin Albu-Schäffer, and Gerd Hirzinger. On joint design with intrinsic variable compliance: derivation of the dlr qa-joint. In *2010 IEEE International Conference on Robotics and Automation*, pages 1687–1694, 2010. doi: 10.1109/ROBOT.2010.5509662.

[9] Thomas G. Sugar. A novel selective compliant actuator. *Mechatronics*, 12(9):1157–1171, 2002. ISSN 0957-4158. doi: https://doi.org/10.1016/S0957-4158(02)00021-1. URL https://www.sciencedirect.com/science/article/pii/S0957415802000211.

[10] Florian Petit, Maxime Chalon, Werner Friedl, Markus Grebenstein, Alin Albu-Schäffer, and Gerd Hirzinger. Bidirectional antagonistic variable stiffness actuation: Analysis, design & implementation. In *2010 IEEE International Conference on Robotics and Automation*, pages 4189–4196, 2010. doi: 10.1109/ROBOT.2010.5509267.

[11] Ronald Van Ham, Bram Vanderborght, Michaël Van Damme, Björn Verrelst, and Dirk Lefeber. Maccepa, the mechanically adjustable compliance and controllable equilibrium position actuator: Design and implementation in a biped robot. *Robotics and Autonomous Systems*, 55(10):761–768, 2007.

ISSN 0921-8890. doi: https://doi.org/10.1016/j.robot.2007.03.001. URL https://www.sciencedirect.com/science/article/pii/S0921889007000371.

[12] Bram Vanderborght, Nikos G. Tsagarakis, Ronald Van Ham, Ivar Thorson, and Darwin G. Caldwell. Maccepa 2.0: compliant actuator used for energy efficient hopping robot chobino1d. *Autonomous Robots*, 31(1):55–65, 2011. ISSN 1573-7527. doi: 10.1007/s10514-011-9230-7. URL https://doi.org/10.1007/s10514-011-9230-7.

[13] E. Dertien. Dynamic walking with dribbel. *IEEE Robotics & Automation Magazine*, 13(3):118–122, 2006. doi: 10.1109/MRA.2006.1678145.

[14] Fares J Abu-Dakka and Matteo Saveriano. Variable impedance control and learning—a review. *Frontiers in Robotics and AI*, 7:590681, 2020.

[15] Manuel Keppler, Dominic Lakatos, Christian Ott, and Alin Albu-Schaffer. Elastic structure preserving impedance (espi)control for compliantly actuated robots. In *2018 IEEE/RSJ International Conference on Intelligent Robots and Systems (IROS)*, pages 5861–5868, 2018. doi: 10.1109/IROS.2018.8593415.

[16] Manuel Keppler, Florian Loeffl, David Wandinger, Clara Raschel, and Christian Ott. Analyzing the performance limits of articulated soft robots based on the espi framework: Applications to damping and impedance control. *IEEE Robotics and Automation Letters*, 6(4):7121–7128, 2021. doi: 10.1109/LRA.2021.3097079.

[17] G.A. Pratt and M.M. Williamson. Series elastic actuators. In *Proceedings 1995 IEEE/RSJ International Conference on Intelligent Robots and Systems. Human Robot Interaction and Cooperative Robots*, volume 1, pages 399–406 vol.1, 1995. doi: 10.1109/IROS.1995.525827.

[18] Sebastian Wolf, Giorgio Grioli, Oliver Eiberger, Werner Friedl, Markus Grebenstein, Hannes Höppner, Etienne Burdet, Darwin G. Caldwell, Raffaella Carloni, Manuel G. Catalano, Dirk Lefeber, Stefano Stramigioli, Nikos Tsagarakis, Michaël Van Damme, Ronald Van Ham, Bram Vanderborght, Ludo C. Visser, Antonio Bicchi, and Alin Albu-Schäffer. Variable stiffness actuators: Review on design and components. *IEEE/ASME Transactions on Mechatronics*, 21 (5):2418–2430, 2016. doi: 10.1109/TMECH.2015.2501019.

[19] B. Vanderborght, A. Albu-Schaeffer, A. Bicchi, E. Burdet, D. Caldwell, R. Carloni, M. Catalano, G. Ganesh, M. Garabini, M. Grebenstein, G. Grioli, S. Haddadin, A. Jafari, M. Laffranchi, D. Lefeber, F. Petit, S. Stramigioli, N. Tsagarakis, M. Van Damme, R. Van Ham, L.C. Visser, and S. Wolf. Variable impedance actuators: Moving the robots of tomorrow. In *2012 IEEE/RSJ International Conference on Intelligent Robots and Systems*, pages 5454–5455, 2012. doi: 10.1109/IROS.2012.6385433.

[20] Sebastian Wolf, Oliver Eiberger, and Gerd Hirzinger. The dlr fsj: Energy based design of a variable stiffness joint. In *2011 IEEE International Conference on Robotics and Automation*, pages 5082–5089, 2011. doi: 10.1109/ICRA.2011.5980303.

[21] Jan Lunze. Regelungstechnik 1, 2010.

[22] Sigurd Skogestad and I Postlethwaite. *Multivariable Feedback Control: Analysis and Design*, volume 2, chapter 2, pages 23–26. Wiley, 01 2005.

[23] Manuel Keppler, Christian Ott, and Alin Albu-Schäffer. From underactuation to quasi-full actuation: Aiming at a unifying control framework for articulated soft robots. *International Journal of Robust and Nonlinear Control*, 32(9):5453–5484, 2022. doi: https://doi.org/10.1002/rnc.6102. URL https://onlinelibrary.wiley.com/doi/abs/10.1002/rnc.6102.

[24] David Wandinger. Enhancing classical impedance control concepts while ensuring transferability to flexible joint robots. Master's thesis, Hochschule München, 09 2020. URL https://elib.dlr.de/139129/.